

REU 2017

BEYOND



Research Experience for Undergraduates

Section 1.5

Support for the REU program is provided by the NSF MRSEC program (DMR-1120296) and the REU Site program (DMR-1460428).

TABLE OF CONTENTS

REU	Faculty Advisor	Page
Buser, Alexander	Prof. Dan Ralph	03
Cremer, Maegan	Prof. Meredith Silberstein	26
David, Philippe	Prof. Paulette Clancy	45
DiTusa, Rebecca	Prof. Chris Xu	65

Radio-Frequency Current Calibration for Spin-Torque Ferromagnetic Resonance in Pt/Py

Alexander Buser¹, Neal Reynolds^{1,2}, and Dan Ralph^{1,2}
Cornell Center for Materials Research¹, Cornell University²

(Dated: August 9, 2017)

In recent years, the burgeoning field of spintronics has yielded a wealth of materials showing great promise for the development of a new generation of magnetic memory devices. Among these materials is a class of nanoscale devices operating on the principle of spin-transfer torque - a way of manipulating magnetic orientation in layers of magnetic material using currents of spin-polarized charge carriers. A common method of characterizing effective generators of spin-transfer torque relies on an experimental technique known as spin-torque ferromagnetic resonance (STFMR). While this technique is fairly robust, its utility can suffer from unreliable calibration methods. In this report we present and verify a calibration method which is simpler and potentially more reliable than current practice.

I. INTRODUCTION

A. Spin-Transfer Torque

The study of spin-transfer torque, the transfer of angular momentum to a magnetic layer via spin-polarized charge carriers, began in the late 1970's with the work of Berger, who first considered the effects of spin-polarized electrons on magnetic domain walls [1]. It was not until more recently, however, that advances in nanofabrication enabled the production of devices exhibiting the effects of spin-transfer torque at low charge currents, opening up the field to a vast array of technological applications [2].

One method of generating spin-transfer torque owes its existence to the phenomenon of spin-orbit coupling. Electrical current through a conductive material with spin-orbit coupling causes the charge carriers to separate based on the orientation of their spins, resulting in spin accumulation at the lateral boundaries of the sample[3]. This process is referred to as the spin Hall effect in analogy with the ordinary Hall effect, in which charge current transverse to an applied voltage is generated by an external field.

By growing a thin magnetic layer (with a thickness on the order of several nanometers) on top of a conductive layer, we can inject angular momentum into the magnetic layer via the spin Hall effect, changing the orientation of its magnetization [3]. The efficiency of this angular momentum injection is typically characterized by a dimensionless figure of merit known as the spin Hall angle (Θ_{SH}), which is calculated as the ratio of the generated spin current to the applied charge current.

B. Spin-Torque Ferromagnetic Resonance

In order to obtain quantitative measurements of Θ_{SH} , we use the technique of spin-torque ferromagnetic resonance (STFMR). Ordinary ferromagnetic resonance is based on the principle of exciting precession of a layer's

magnetization by applying a magnetic field oscillating at radio-frequency (RF). In STFMR, spin-transfer torque generated by the spin Hall effect, rather than an external field, excites precession of the magnetization.

To carry out this measurement, we use an RF signal generator to run current through a device composed of a bilayer of a spin Hall metal and a magnetic layer several nm thick. The amplitude of the RF signal is modulated in the kilohertz range and fed to a lock-in amplifier which measures the voltage across the device through a bias tee. Spin-transfer torque generated by the conducting layer and the magnetic field induced by the RF current cause the magnetic layer's magnetization to precess about the direction of a large (up to approximately 0.2 T) external magnetic field. As the magnetization of the magnetic layer precesses about the external field, anisotropic magnetoresistance (AMR) causes the resistance of the device to alternate at radio-frequency. The resistance of the device mixes with the applied current to produce a voltage oscillating at the kilohertz range frequency of the amplitude modulation of the RF signal which is picked out by the lock-in amplifier.

The magnetization dynamics are described by the Landau-Lifshitz-Gilbert-Sloczewski (LLGS) equation [4]. Solving the LLGS equation for the motion of the magnetization yields an expected measured voltage as a function of external magnetic field strength given by the sum of a symmetric and an antisymmetric Lorentzian, a type of distribution characteristic of resonance phenomena [5];

$$V_{mix} \propto I_{RF} [SF_S(H_{ext}) + AF_A(H_{ext})]. \quad (1)$$

Here I_{RF} is the magnitude of the RF current through the device, and S and A are the amplitudes of the respectively symmetric and antisymmetric Lorentzians;

$$F_S(H_{ext}) = \frac{\Delta^2}{\Delta^2 + (H_{ext} - H_0)^2}$$
$$F_A(H_{ext}) = F_S(H_{ext})(H_{ext} - H_0)/\Delta,$$

where Δ and H_0 are fitting parameters representing the linewidth of the resonance curve and external field

strength at which resonance occurs, respectively. Sweeping the strength of the external field and fitting the mixing voltage to the form above, we obtain measurements of S , A , Δ , and H_0 .

Analytical solutions of the equations of motion predict that the symmetric amplitude arises from a torque oriented in the plane of the layer (such as that due to the spin-transfer torque), while the antisymmetric amplitude has its origins in the out-of-plane component (including that from the magnetic field induced by the RF charge current, referred to as the Oersted torque). In the absence of other out-of-plane torques, the spin Hall angle Θ_{SH} is directly proportional to the ratio of the symmetric and antisymmetric amplitudes S/A [5].

II. RF CURRENT CALIBRATION METHODS

While many devices, including the bilayer platinum permalloy (Pt/Py, Py = Ni₈₁Fe₁₉) devices considered here, demonstrate no significant out-of-plane torque apart from the Oersted torque, some materials exhibit additional out-of-plane torques arising from spin-orbit coupling [5, 6]. In these cases, we must determine the portion of the antisymmetric amplitude due to the Oersted torque in order to calculate the spin Hall angle.

We can directly relate the magnitude of the charge current to the antisymmetric amplitude of the mixing voltage due to the Oersted torque using Ampere's law. Knowing the amount of charge current through the device will therefore allow us to calculate the spin Hall angle of the magnetic layer. When applying RF current, however, we must account for the difference in supplied and incident current arising from impedance mismatch between the device and RF network and losses throughout the network of cables.

A. Vector Network Analyzer

A standard method for determining how much RF current reaches a load uses a vector network analyzer (VNA). Upon calibrating our vector network analyzer (Agilent 8722ES) with a standard 50 Ohm calibration kit, we conduct measurements of the reflection coefficient of each device and transmission coefficient for the entire network for a range of RF frequencies. These quantities capture the leading contributions to RF power loss, allowing us to determine the amount of current through a given device [3].

This method, however, possesses a large degree of uncertainty owing to the fragility of RF equipment and sizable variations across VNA calibrations, as shown in Figure 1. Furthermore, vector network analyzers are prohibitively expensive, and unsuited for use in experiments involving wire bonded electrical contacts which cannot be connected and disconnected reproducibly, as is necessary in order to conduct measurements of the reflection

and transmission coefficients.

B. DC Heating Method

An alternative method of obtaining the amount of current through a device without using a vector network analyzer was recently put forward by Tshitoyan et. al [7]. In [7], the authors measure the resistance of a given device for a range of DC currents and then for a range of RF powers. By comparing the resistance for a given applied RF power to the DC current which produces the same resistance, the amount of RF current reaching the device can be deduced.

In our attempts to use the method in [7], however, we had difficulty achieving reproducible results with sufficiently high signal to noise. This was likely due to the lower resistances of our devices and the smaller changes in resistance measured for a given frequency, owing to the different materials we were using. We find more robust results by applying a slightly different method. Instead of directly mapping the resistances measured for a given RF power to the resistance measured for the corresponding DC current, we perform linear regression on resistance vs. power data for applied DC and RF currents at a range of frequencies. The ratio of the slope of the RF power vs. resistance curve for a given frequency and that of the corresponding DC curve determines the amount of RF power that reaches the device (see Figure 2).

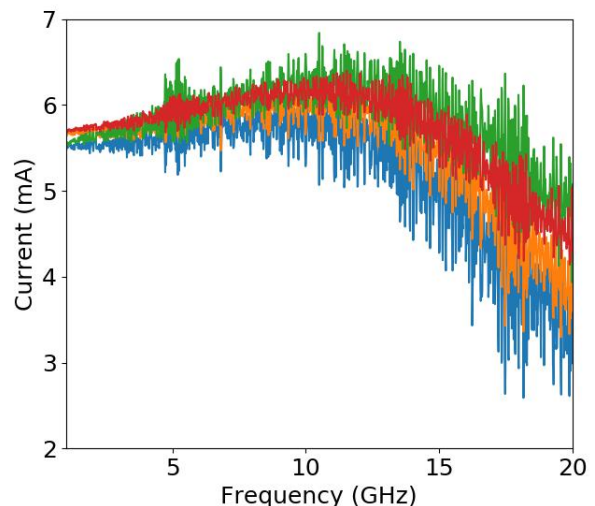


FIG. 1. Current through a device determined by three independent measurements of the reflection coefficient S_{11} (dB) using different VNA calibrations (distinguished by color). The considerable variation across calibrations points to the inaccuracy of the VNA method for devices with large values of S_{11} .

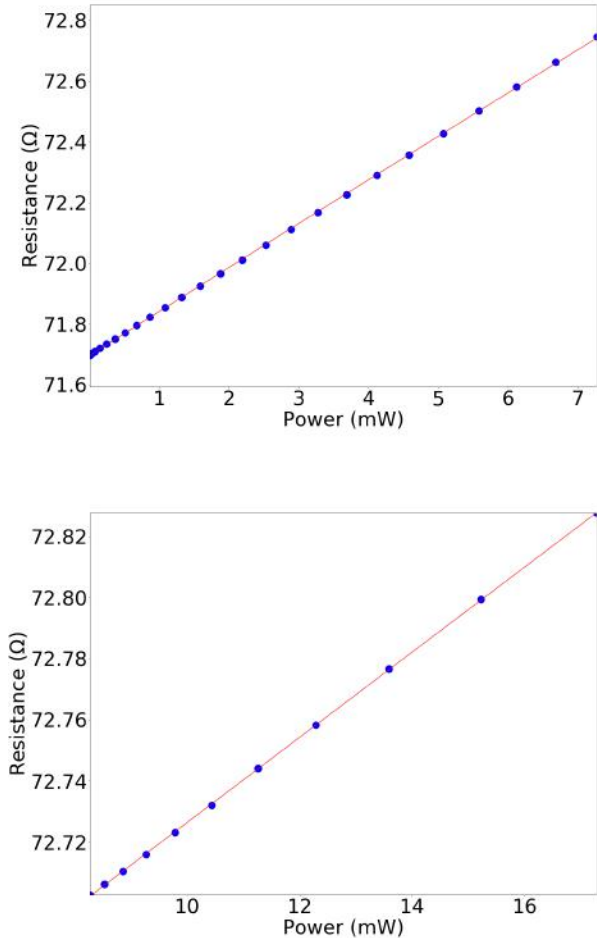


FIG. 2. **Top:** Resistance versus applied DC power and fit by linear regression. We assume no DC power loss through the network of cables. **Bottom:** Resistance versus applied RF power and linear fit at 10 GHz - the ratio of the slopes between the two plots is used to determine the fraction of RF power reaching the device.

III. RESULTS

We carried out measurements on a series of bilayer devices composed of a 5.4 nm thick layer of platinum capped by a 6 nm permalloy magnetic layer and 2.2 nm hafnium layer (to minimize oxidization) grown using dc magnetron sputter deposition on *c*-axis oriented sapphire substrate. The devices were fabricated into rectangular geometries of varying aspect ratio with dimensions typically on the order of tens of microns. Electrical contact to the devices was made with sputter Pt leads in a coplanar waveguide configuration to minimize RF power loss.

Our modification to the heating calibration method in [7] described above was carried out three times on the same 12 μm by 6 μm Pt/Py device (with current applied along the 12 μm dimension). DC current was swept from

-10 mA to 10 mA and the resulting power calculated using the resistance of the device at zero applied current, as the change in resistance was found to be negligible compared to the resistance of the device (Fig. 2 Top). The resistance vs. current curve was symmetrized in order to eliminate the effects of a DC voltage offset produced by the source meter used to measure resistance. RF current was applied to the same device using a frequency generator (Agilent 8257D), and the power swept from 0 to 10 dBm with frequency varying from 1 to 20 GHz. A sizable 10 mA DC current was applied simultaneously with RF current, as this was found to lead to more robust results.

Using a vector network analyzer, we observed a reflection coefficient (S_{11}) on the order of -17 dBm for this device indicating little RF power is lost due to impedance mismatch with the device. The majority of RF power lost is thus dissipated by the network of cables. The dominant source of uncertainty in the VNA method described earlier in Fig. 1 is thereby eliminated, as the calibration method used to determine S_{11} is largely irrelevant. This enables us to directly compare the results of the DC Heating method to the transmission coefficient reported by the VNA in order to establish agreement between the two methods. As shown in Figure 3, there is reasonable agreement between them, particularly at RF frequencies above 10 GHz.

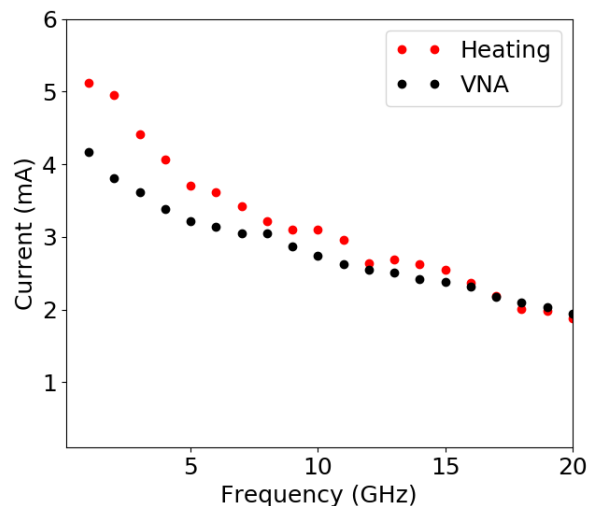


FIG. 3. RF current through a 12 μm by 6 μm Pt(6 nm)/Py(5.4 nm) STFMR device as reported by VNA and determined using the DC heating method for a 10 dBm applied signal. The VNA curve was determined by averaging S_{21} across five independent calibrations, while the heating data was obtained by averaging across three trials on the same device.

Having effectively calculated the transmission coefficient of the RF network using the DC heating method, we calculated the spin Hall angle of the device by carrying out spin-torque ferromagnetic resonance measurements. STFMR experiments were carried out with the swept ex-

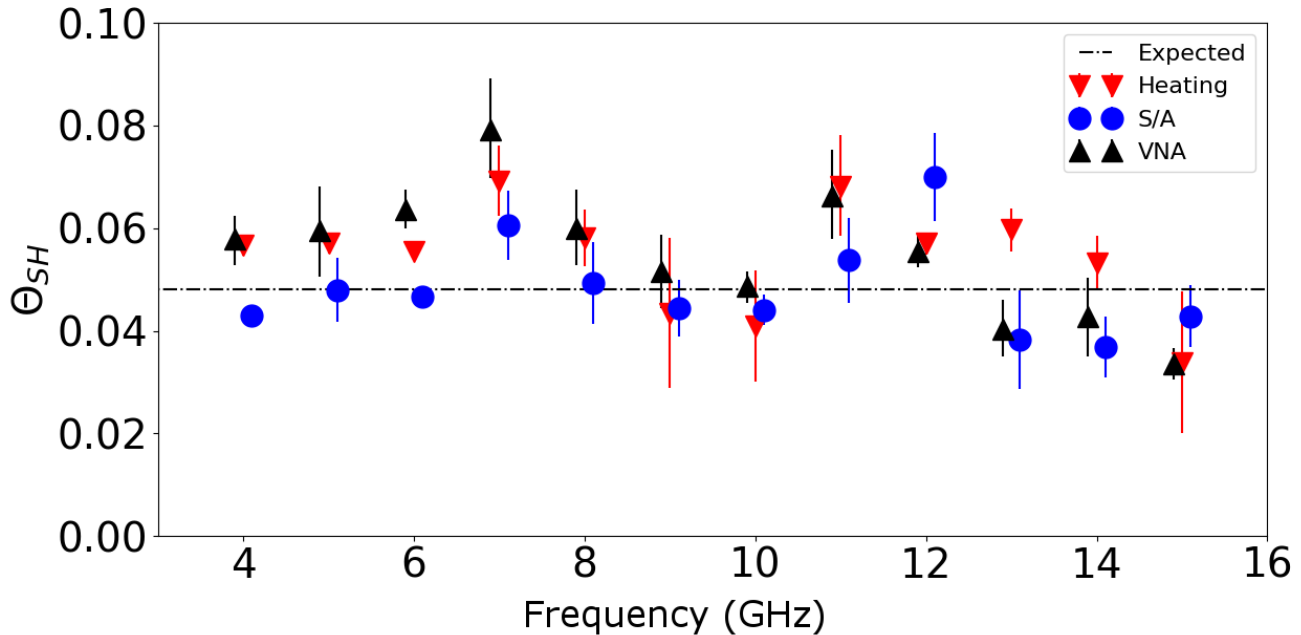


FIG. 4. Spin Hall angle of a 12 μm by 6 μm Pt(6 nm)/Py(5.4 nm) STFMR device using three different methods; S/A refers to the ratio of the symmetric and antisymmetric components of the mixing voltage. Error bounds determined by repeated STFMR trials. Expected value (dashed line) shown as mean of S/A data across all frequencies - this value agrees with expected results for Θ_{SH} in platinum. Heating method results were found to have a mean closer to the expected value and lower standard deviation than those of the VNA.

ternal, in-plane field at 45 degrees from the direction of current flow in the device to maximize signal. We determined the magnitude of the AMR by measuring the resistance of the device as a function of the angle of an applied, static 0.2 T in-plane field from 0 to 360 degrees relative to the direction of current flow.

IV. CONCLUSIONS

We have shown that the DC heating method and vector network analyzer give similar results for Pt/Py STFMR devices. These results are validated by their agreement with the Θ_{SH} calculated by S/A (see Figure 4), which

should be correct in the Pt/Py system [5]. The consistent variation of the spin Hall angle with frequency across the three techniques also highlights that the agreement between the calibration methods is greater than the systematic error in the experiments. Based on these results, then, it seems the heating method is a viable alternative for experimental setups involving wirebonded electrical contacts, which cannot be connected and disconnected reproducibly in order to conduct measurements using a VNA. Furthermore, we expect the heating method to give more reliable results than the VNA for devices with large values of S_{11} (*i.e.* having a large impedance mismatch), as the variation across S_{11} calibrations is a leading source of error in VNA measurements.

-
- [1] L. Berger. Low-field magnetoresistance and domain drag in ferromagnets. *Journal of Applied Physics*, 49:2156–2161, March 1978. doi:10.1063/1.324716.
- [2] D. C. Ralph and M. D. Stiles. Spin transfer torques. *Journal of Magnetism and Magnetic Materials*, 320:1190–1216, 2008. doi:10.1016/j.jmmm.2007.12.019.
- [3] A. Mellnik. *Measurements Of Spin Torques Generated By Topological Insulators and Heavy Metals*. PhD thesis, Cornell University, 2015.
- [4] J.C. Slonczewski. Current-driven excitation of magnetic multilayers. *Journal of Magnetism and Mag-*

- netic Materials*, 159(1):L1 – L7, 1996. ISSN 0304-8853. doi:http://dx.doi.org/10.1016/0304-8853(96)00062-5. URL <http://www.sciencedirect.com/science/article/pii/0304885396000625>.
- [5] Luqiao Liu, Takahiro Moriyama, D. C. Ralph, and R. A. Buhrman. Spin-torque ferromagnetic resonance induced by the spin hall effect. *Phys. Rev. Lett.*, 106:036601, Jan 2011. doi:10.1103/PhysRevLett.106.036601. URL <https://link.aps.org/doi/10.1103/PhysRevLett.106.036601>.

- [6] Neal Reynolds, Priyamvada Jadaun, John T. Heron, Colin L. Jermain, Jonathan Gibbons, Robyn Collette, R. A. Buhrman, D. G. Schlom, and D. C. Ralph. Spin hall torques generated by rare-earth thin films. *Phys. Rev. B*, 95:064412, Feb 2017. doi: 10.1103/PhysRevB.95.064412. URL <https://link.aps.org/doi/10.1103/PhysRevB.95.064412>.
- [7] V. Tshitoyan, C. Ciccarelli, A. P. Mihai, M. Ali, A. C. Irvine, T. A. Moore, T. Jungwirth, and A. J. Ferguson. Electrical manipulation of ferromagnetic nife by antiferromagnetic irmn. *Phys. Rev. B*, 92:214406, Dec 2015. doi: 10.1103/PhysRevB.92.214406. URL <https://link.aps.org/doi/10.1103/PhysRevB.92.214406>.

Synthesis of Force Responsive Methacrylate Copolymers by Maegan Ashley Cremer

Abstract:

Marine biofouling is the accumulation of algae, soft corals, diatoms, and barnacles on the bottoms and hulls of vessels. The growth of these fouling pests increases the drag on the vessel thus increasing its fuel consumption over time. We propose a force responsive methacrylate copolymer characterized by acid-base dimers. These dimers would reversibly polarize and break under strain to produce a change in surface energy. Such a material would move from hydrophobic in its native state to hydrophilic under strain. This strain would be created by drag forces or adhesion of fouling pests which would de-bond in response to the change in surface energy.

Acidic, basic, and tri-copolymers were synthesized in toluene and in bulk with a cross-linking agent. The resulting materials were characterized with proton NMR, ATR-FTIR, and contact angle. Contact angle measurements were taken in static and strained states. Spontaneous gelation reactions were observed after synthesis in toluene. The bulk synthesis materials exhibited increases in brittle behavior with increasing percentages of charged groups making them untestable in tension. ATR-FTIR indicates successful synthesis of the materials through the bulk polymerization method. The contact angle data is largely inconclusive.

Introduction

Marine biofouling is the accumulation of species such as diatoms, protozoa, soft corals, barnacles, and muscles on submerged surfaces [1]. The character of these surfaces is dependent upon a number of factors—the species in the fouling community and the geographic location—which ultimately affect the topology of the surface [1]. Biofouling decreases ship speed and efficiency by contributing to frictional drag thereby increasing the amount of energy and fuel required to propel the vessel [2]. The greatest financial cost accrued by biofouling is the increase in fuel consumption [2]. In an economic analysis performed by Schultz et. al., heavy slime alone (FR-30 by NSTM fouling ratings) results in a 10.3% increase in fuel consumption, while small hard fouling organisms (FR-60) results in a 20.4% increase in fuel consumption. Most vessels are expected to foul within 5 years of use [3].

Researchers have taken a variety of approaches to solve the biofouling conundrum. The development of antifouling surfaces can be either biocidal or fouling resistant. Biocidal surfaces kill adsorbed organisms while fouling resistant surfaces

deter attachment [1]. In the past, antifouling paints contained toxic leachates such as tributyltin oxide, lead, and arsenic the use of which has been largely discontinued [1, 4]. The study of bioadhesives utilized by fouling organisms has led researchers to alternative antifouling strategies: surface topology and surface energy [1]. Surface characteristics are important to organism's ability to recognize and adhere to the surface. Patterns such as that on the lotus leaf create super hydrophobic surfaces that are unfavorable for adhesion of micro-organisms [5]. Similarly, the pattern on shark skin is unfavorable for the colonization of fouling pests [6]. This pattern has been replicated on PDMS by Dr. Brennan at the University of Florida and has been proven to function as an anti-fouling surface [6]. Unfortunately, micro-patterning of silicone is not a durable solution [1, 6].

We propose a dynamic polymeric coating which would respond to the increased drag generated by fouling organisms. The initially hydrophobic surface would shift to a hydrophilic, unfavorable binding surface with the application of strain. To accomplish this, we are investigating polymeric materials with ionic cross-linking behaviors. Dimers formed between acidic and basic monomers—carboxylate and amine respectively—would

deform or break with strain creating local polarity and an increase in surface energy. A blend of acidic and basic polymers are synthesized and investigated for intermolecular cross-linking behavior. Intramolecular cross-linking is explored through use of a tri-copolymer consisting of a hydrophobic monomer, acidic monomer, and basic monomer. This process should be reversible in nature as the dimers would reform with release of the applied strain.

Materials & Methods

Acidic, basic, and tri-copolymers were synthesized two ways: with purification of monomers and bulk polymerization. In the first process—with the purification of monomers—the intention is to develop thermoplastics which would be washed and blended in different concentrations. The acidic and basic polymers would be combined affording exploration of interchain ionic cross-linking relative to the tri-copolymer intra-chain ionic behavior. The bulk polymerization of the same monomeric species utilizes a cross-linking agent to control for cross-linked behavior.

Materials: All monomers and solvents were obtained from Sigma Aldrich. Monomers 2-ethylhexyl methacrylate (2-EHMA) and 2-(dimethylamino)ethyl methacrylate were cleaned using basic alumina and cotton wool to remove inhibitor prior to use. 2-(dimethylamino)ethyl methacrylate, mono-2-(methacryloyloxy)ethyl succinate, and azobis-(isobutyronitrile) (AIBN) were stored at 4°C prior to use. Toluene, ethyl acetate, and methanol were used as received.

Thermoplastic Polymer Synthesis:

Polymers were prepared through free-radical polymerization purged with nitrogen. Three types of polymers were synthesized: acid, base, and random tri-copolymer. Toluene—purged with nitrogen—is mixed with 2-EHMA and other monomers per table 1 in a 60mL scintillation vial with stir bar. AIBN, initiator, is dissolved in 3mL of toluene then added drop wise to the reaction. After the addition of initiator, the vials are placed in a silicone

oil bath which begins heating to 65°C. Temperature is monitored with a thermometer till stable. Nitrogen continues to bubble through the reaction for one hour before the vials are capped. The reaction is allowed to proceed overnight. Reaction structures are depicted in appendix A.

Table 1. Quantities for Synthesis of Thermoplastic Polymers

	2EHMA (mL)	Base (g)	Acid (mL)	AIBN (g) (0.5%)	Toluene (mL)
5% base	10	0.5	x	0.039	30
5% acid	10	x	0.5	0.039	30
10% base	10	1.0	x	0.042	30
10% acid	10	x	0.959	0.041	30
20% base	10	2.0	x	0.047	30
20% acid	8	x	2	0.038	30
5% tri-copolymer	13	0.25	0.308	0.05	45
10% tri-copolymer	13	0.5	0.616	0.053	45
20% tri-copolymer	13	1.18	1.45	0.060	45

Table 1. Base is 2-(dimethylamino)ethyl methacrylate, acid is mono-2-(methacryloyloxy)ethyl succinate.

Post Processing:

The polymer is transferred to a round bottom flask for washing. First the toluene is evaporated using a rotovap with an ice and water mixture in the condenser and a 50°C water bath. Polymer is then washed with bad solvent 3:1 by volume—according to table 2—with swirling to induce phase separation. The washed polymer is allowed to settle to the bottom of the flask and the rinseate decanted. Remaining solvent is evaporated from the polymer using the rotovap. The dried polymer is then dissolved in favorable solvent listed in table 2 and the process repeated three times. The washed polymer was cast into a teflon mold and allowed to dry in the fume hood overnight.

Table 2. Post-processing Solvents

	good solvent	bad solvent
5% base	ethyl acetate	methanol
5% acid	ethyl acetate	methanol
10% base	toluene	methanol
10% acid	toluene	methanol
20% base	ethyl acetate	methanol
20% acid	ethyl acetate	methanol or hexane
5% tri-copolymer	toluene	methanol
10% tri-copolymer	toluene	methanol
20% tri-copolymer	ethyl acetate	methanol

Cast polymer was dried further in a vacuum oven set to 80°C under nitrogen overnight. Temperature was then increased to 120°C and vacuum pulled to -0.08 MPa. After 5 hours, the temperature was increased to 140°C and vacuum pulled to -0.1 MPa overnight. Prior to removal from the oven, temperature was decreased to 60°C and the chamber purged with nitrogen.

Casting for testing: For mechanical testing, 2.5 grams of polymer are placed in a PDMS mold and heated in a vacuum oven (140°C and -0.1MPa overnight) to create an even block of material. For contact angle, 2 grams of polymer are placed in a teflon mold 5cm in diameter and heated in a vacuum oven (140°C, -0.1 MPa overnight) to form an even block of material. Samples are then cut to allow for unobstructed imaging.

Acid Polymer Synthesis via Hydrolysis:

Poly-2EHMA, prepared according to the thermoplastic polymerization method previously described, is dissolved in a round bottom flask with toluene heated to 110°C. This takes about 20 minutes. Combine with concentrated solution of potassium hydroxide (KOH) to form carboxylic acid shown in figure 1. The amount of carboxylic acid was controlled by the amount of KOH introduced. 10 and 20% carboxylate polymers were generated in this fashion. Reaction is allowed to proceed overnight with a condenser to prevent loss of toluene.

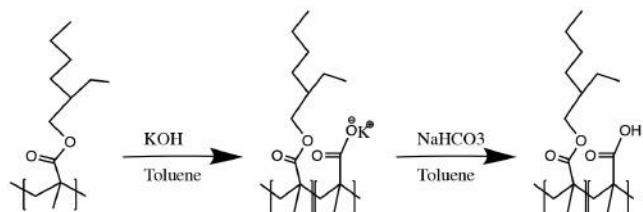


Figure 1. A schematic detailing the hydrolysis and protonation of poly-2EHMA to form a carboxylic acid.

Using a separatory funnel, potassium is washed from the polymer by protonating the carboxyl with excess 1M hydrochloric acid (HCl). The polymer is then washed with DIW 3 times. The resulting polymer is then washed with methanol as described in post processing.

For analysis with FTIR, the samples deprotonated using a saturated solution of sodium bicarbonate (Sigma Aldrich). Samples were dissolved in toluene, exposed to the water-sodium bicarbonate solution, and separated.

NMR: 10 mg of polymer were dissolved in 2-3 mL of chloroform. The chloroform was evaporated from the sample by placing the vial in a hot water bath (65°C) over night. The dry polymer sample was then dissolved in 0.7 mL deuterated chloroform and transferred to a NMR tube. (NMR machine specifications: Samples were analyzed with proton and carbon 13 NMR. carbon 13 scans ran for 1 hour)

Contact Angle:

Contact angle measurements are taken using the sessile drop method, a goniometer (12 frames per second for 10 seconds), and the following three liquid phases: deionized water (DIW), light mineral oil (Aldrich), and 3.5% NaCl (stark solution 26% NaCl from Sigma Aldrich) in DIW. 5 drops are measured with each liquid phase. The contact angle is evaluated using the Young-Laplace form for an established base line. The values collected for each test drop are averaged with respect to time to provide a single average contact angle verses time model. The contact angle of the surfaces is

measured a second time after the material has been strained in uniaxial tension. This data is processed in the same way as the static contact angle.

Bulk polymerization:

Three species of polymer were created with this method: acidic, basic, and tri-copolymer. The quantities and ratios of the species utilized for each sample are described in table 3. Monomers are not purified prior to synthesis. Cross-linker (tetra(ethylene glycol) diacrylate) (Sigma) and, if applicable, basic monomer (2-(dimethylamino)ethyl methacrylate) are weighed in a vial. The hydrophobic monomer (2EHMA) and, if applicable, acidic monomer are added to the reaction volume and swirled. Initiator (AIBN) is weighed and added to the reaction. The reaction volume is then purged with nitrogen for thirty minutes and capped. The sealed vial is placed on a hotplate with a surface temperature of 70-75°C and swirled occasionally. When a visible change in viscosity occurs, the polymer is cast into a teflon mold and allowed to polymerize overnight. The samples are then dried in a vacuum oven at temperatures increasing from 115 to 140°C under nitrogen over a period of 24 hours. The structures for the reactions are given in appendix B.

Table 3. Quantities for Bulk Polymerization

	2EHMA (mL)	Base (g)	Acid (mL)	AIBN (2%) (g)	Crosslinker (1%) (g)
5% base	3	0.11	x	0.047	0.042
5% acid	3	x	0.15	0.047	0.043
5% tricopolymer	3	0.06	0.069	0.046	0.043
10% base	3	0.25	x	0.05	0.045
10% acid	3	x	0.287	0.049	0.045
10% tri-copolymer	3	0.12	0.144	0.049	0.045
20% base	3	0.55	x	0.05	0.051
20% acid	3	x	0.67	0.055	0.051
20% tri-copolymer	3	0.27	0.33	0.055	0.051
40% tri-copolymer	3	0.7	0.86	0.073	0.067

ATR-FTIR: No additional sample preparation was required for ATR-FTIR.

Titration with methyl purple:

To evaluate the success of the hydrolysis reaction to create the carboxylate polymer, a titration with methyl purple in THF was developed. Dissolve methyl purple (BICCA) and polymer in tetrahydrofuran (THF) (Honeywell) and dropper methyl purple-THF into the polymer. Reversibility of the reaction tested with triethyl amine (Et3N)(Sigma). Acidity of the polymer is compared to dilute solutions of acetic acid.

Results and Discussion

Due to spontaneous gelation reactions at various stages of the project not all samples were testable at all stages, largely inconclusive data were collected on the thermoplastic synthesis.

Synthesis and Characterization of Thermoplastic Materials:

Gelation reactions: Polymers synthesized according to the thermoplastic synthesis experienced spontaneous gelation reactions. Initially, heating of the materials to 140°C in an aerobic environment was correlated with cross-linking. The materials would not spread in PDMS molds upon heating and would swell when placed in toluene or ethyl acetate. Cross-linked materials were re-synthesized and carefully dried under nitrogen. The materials behaved as gels upon drying. The materials swelled in ethyl acetate are seen in appendix C. At this time there had been a shift in manufacturer (TCI) for the hydrophobic monomer—2-ethylhexyl methacrylate. Polymers were prepared a third time with fresh hydrophobic monomer from Sigma. Materials again behaved as gels upon drying. This behavior is seen in appendix D where the material is pictured with an uneven surface and not spreading in PDMS mechanical testing molds nor in teflon contact angle molds. The acidic monomer was analyzed with proton NMR and was found not to contain methacrylate dimers. The presence of methacrylate dimers would

have caused the observed cross-linking behavior.

Contact Angle:

Both water and oil droplets on the needle are attracted to the surfaces of basic and tri-copolymers. As the polymer is moved underneath the test liquid the droplet can be seen moving toward the polymer surface. The sequence of images in figure 2 illustrate the attraction between a droplet of light mineral oil and 5% tri-copolymer (2.5% of acid and 2.5% base). No attractive behaviors are seen with polymers consisting of only hydrophobic monomer or carboxylic moieties of any concentration. These materials were not testable beyond attraction behavior due to uneven surfaces.



Figure 2: Still images taken from a video of light mineral oil being attracted to the edge of a 5% tri-copolymer sample. The polymeric material is seen approaching from the right. The test liquid is seen being pulled off its central axis and drawn to the surface.

Acid Polymer Synthesized with Hydrolysis

Titration of hydrolyzed polymer with methyl purple in THF:

The pH indicator, methyl purple, was soluble in THF as expected. The solution changed from blue-green (fig.3a.) to yellow-green as shown in figure 3d when methyl purple in THF was added to the dissolved polymer. Organic base, triethyl amine, was able to successfully titrate the dissolved polymer solution to a light blue-green color (fig. 3e). A control was executed using acetic acid in

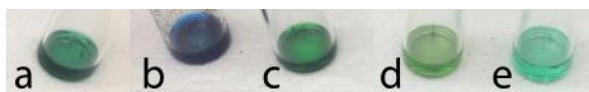


Figure 3: Photographs of the titration with methyl purple in THF. (a) methyl purple in THF, (b) acetic acid with methyl purple and THF, (c) acetic acid with methyl purple, THF, and triethyl amine, (d) polymer in THF with methyl purple, and (e) polymer in THF with methyl purple and triethyl amine.

THF. A solution of acetic acid, THF, and methyl purple yielded a dark blue color (fig. 3b) which was successfully titrated with an organic base, triethyl amine, to a blue-green color (fig.3c.). Increasing amounts of polymer were dissolved in THF to achieve greater concentrations of acid (mac-2, 10% acid). However, when testing the solutions with methyl purple only yellow-green colors appeared. We were unable to replicate the acetic acid results with polymer solutions. Ultimately, this titration was not sufficient in characterizing the concentration of acid in the polymer.

NMR & ATR-FTIR of Hydrolyzed Polymer:

Proton NMR spectra were taken of 10% and 20% hydrolyzed polymer as well as 20% amine polymer (figures 4, 5, and appendix E. 1 respectively). These spectra were compared to spectra of the monomer created by ChemDraw (appendix E). The peaks seen at 0.8, 1, 1.3, 1.5, 1.8, 3.8, and 7.2 ppm are associated with the hydrophobic monomer as they are noted in both the basic polymer spectra and the hydrolyzed sample. Peaks at 0.8, 1, 1.3, 1.5, and 1.8 ppm are indicative of the alkyl components of the side chains. The peak at 3.8 is likely associated with the sp³ carbon adjacent to the oxygen in the hydrophobic monomer. The wide peaks seen at 2.3 and 2.5 ppm in the spectra for the 20% amine polymer are consistent with methyl groups on the amine monomer (figure 5 and appendix E). The peak seen at 4.1 ppm (figure 5) is likely associated with the minor differences between the sp³ carbon adjacent to the oxygen in the amine side group from that in the hydrophobic side group. Peaks seen for the samples are shifted in comparison to the hypothetical spectra created by ChemDraw because of local

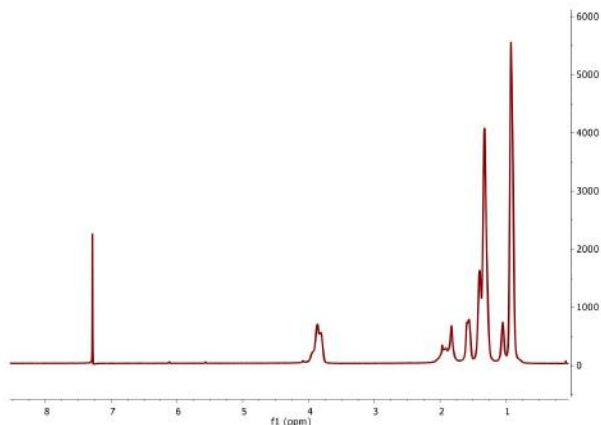


Figure 4. Proton NMR of 10% acid via hydrolysis. No acid peaks are seen and the peak associated with the hydrophobic monomer has not decreased.

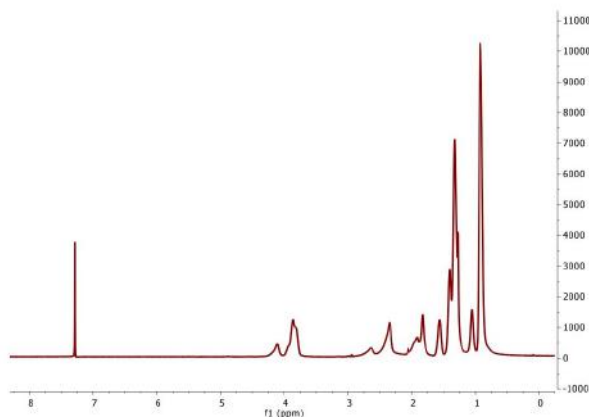


Figure 5. Proton NMR of 20% basic polymer synthesized through the thermoplastic method. Peaks at 2.3, 2.5, and 4.1 are consistent with the predicted spectra for the amine monomer.

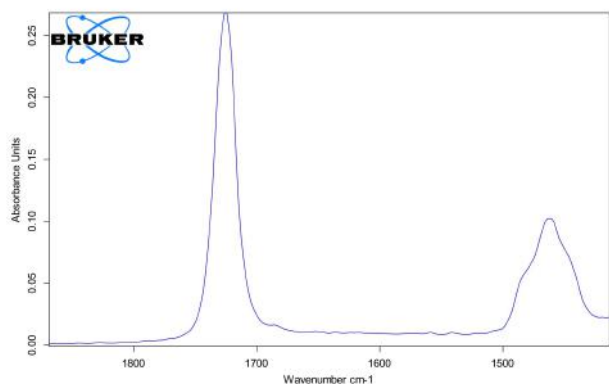


Figure 6. ATR-FTIR of 10% acidic polymer synthesized through hydrolysis. The lack of a peak at 1625 wavenumbers suggests the synthesis was unsuccessful.

environmental shifts in polymer structures with tacticity. The spectra obtained for the hydrolyzed species (figures 4 and appendix E.1.) do not show a decrease in the peak at 3.8ppm nor an appearance of a peak around 12ppm associated with a carboxyl hydrogen. Therefore, the hydrolysis reaction is not considered successful.

ATR-FTIR of 20% hydrolyzed polymer didn't show a peak at 1625 wavenumbers, figure 6. This peak is associated with successful synthesis of the acid functionality.

Bulk Synthesis

Observations: The synthesis proceeds in air only after polymerization has been induced under nitrogen. A sample prepared without this critical step—pictured in appendix F.1.—presented a yellow-orange color and evaporated on the hotplate overnight without exhibiting any visible change in viscosity. Polymers cast into PDMS molds without a great visible viscosity change (approximately the visual viscosity of a simple syrup rather than honey) infiltrated the mold as pictured in appendix F.2.

Many of the polymers took a rose to gold color prior to changes in viscosity; an instance of which is pictured in appendix F.3. This change was not consistent from one synthesis of a polymer to the next. In other instances, the polymer gained a golden or orange color upon drying seen in appendix F. 4. Tri-copolymers (5, 10, and 20%) and basic polymers (5 and 20%) developed rafts (appendix G) upon cooling likely resulting from shrinking of the cross-linked materials. Those which did not produce rafts were cast at greater viscosities.

Contact angle:

Contact angle measurements were completed with light mineral oil (Fischer). Oil was selected as the primary test liquid as its nonpolar character would not interfere with the formation or breaking of ionic dimers in the materials' surface. The material surface was contaminated with oil and thus untestable with other test liquids. Both tri-copolymer and basic polymers exhibited

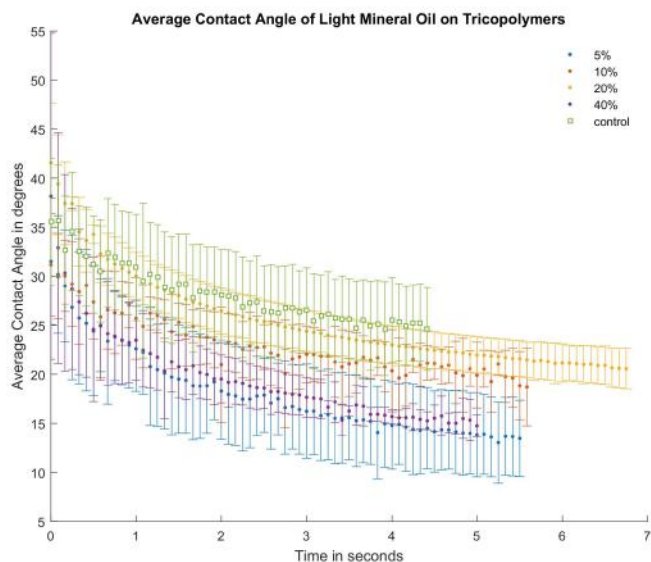


Figure 7. The average contact angle of light mineral oil on tri-copolymers versus time. All materials exhibit rapidly decreasing contact angles over the first 3 seconds of data collection. All data sets fall within range of the control.

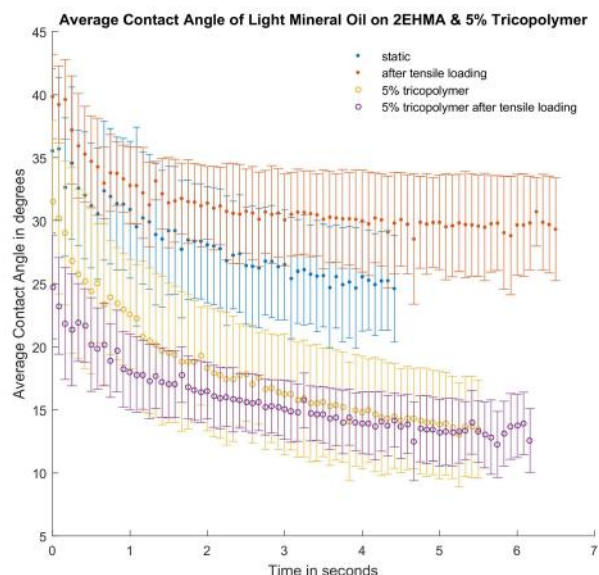


Figure 8. The average contact angle of light mineral oil on 2EHMA and 5% tri-copolymer before and after strain. The contact angle measurements taken after straining the materials fall within their static counter parts.

attraction to the oil test liquid. Acidic polymer and hydrophobic polymer (control) did not exhibit attraction to the test liquid. Average static contact angles for acidic,

basic, and tri-copolymers fall within the control as seen in appendices H.1. and H.2., and figure 7 respectively. A decrease in contact angle with time is seen for all polymers achieving a plateau between 23 and 15° after 3 or 4 seconds. If allowed to stand for one minute, the light mineral oil completely wets all polymer surfaces. This could be due to a highly dynamic surface which is able to maximize favorable interactions with the test liquid or absorption of the test liquid into the surface. Double testing locations on the polymer surface did not exhibit any change in this behavior. It was expected that if the polymer was absorbing the test liquid, then the surface would have been saturated after the first contact thus providing a more stable reading on the second test.

Basic polymers (5%, 10%, and 20%), 5% acidic polymer, and 5% tri-copolymer (2.5% acid and 2.5% base) were measurable after tensile loading. 10 and 20% acidic polymer samples wet to rapidly to be measured, though rapid wetting behavior occurred for all samples tested in tension. 10, 20, and 40% tri-copolymer were too brittle to test in tension. The 10% tri-copolymer sample snapped before visible plastic deformation occurred. The higher percentage tri-copolymer species shattered when cut. The brittle character of the higher percentage tri-copolymers can be attributed to higher degrees of ionic cross-linking between acidic and basic side groups. Synthesis and casting for mechanical testing is required to quantify the increase in modulus.

Of the samples testable in tension, all polymers fell within the control when compared to their static state as illustrated in figure 8 and appendices H.3.- H.5. There is no statistically significant change between the static condition and the tensile condition for the testable materials. This is largely expected for the acidic and basic polymers alone as they do not possess the acid-base dimer suspected to respond to strain. The 5% tri-copolymer exhibiting no change in hydrophobicity or oligophilicity with strain is understandable when considering the percentage of charged species present in the material: 2.5% of each charged species.

This material's similarity to the hydrophobic homopolymer control is clearly illustrated in ATR-FTIR (appendix H.6.).

ATR-FTIR:

IR spectra of the polymers suggests successful synthesis. The basic polymers display peaks at 2770 and 2810cm⁻¹—most visible in the 10 and 20% amine polymers in figures 9 and 10 respectively—which disappear in the tri-copolymers. The disappearance of these peaks is consistent with the shift of an amine participating in hydrogen bonding or cross-linking. The behavior of this bond and corresponding peak could be refined by characterizing the polymer at lower temperatures. The reduced temperature would slow the rate of oscillation between bonding states. Studies performed by Teo et. al. investigated the influence of increasing temperature on hydrogen bonding character in polyurethanes finding broadening of the amine ATR-FTIR peaks with increasing temperature [7]. No significant change was noted for carbonyl groups with increasing temperature [7].

The tri-copolymer spectra show decreased absorbance, relative to their analogous acidic or basic polymers, for wave numbers corresponding to the aliphatic portions of the hydrophobic monomer (2800 through 3000). The decreased absorbance in this region between tri-copolymers is shown in figure 11. This supports successful incorporation of the basic monomeric species during synthesis.

Conclusions and Future Directions

The cause of the gelation reactions in the thermoplastic synthesis is unclear. Inclusion of an inhibitor such as MEHQ after synthesis or post-processing could prevent reactions between side groups or unreacted species. ATR-FTIR of samples before and after gelation may provide some information about changes in structure, however it is not clear how to control for these states.

Bulk synthesis of methacrylate copolymers with tetra(ethylene glycol) diacrylate as a

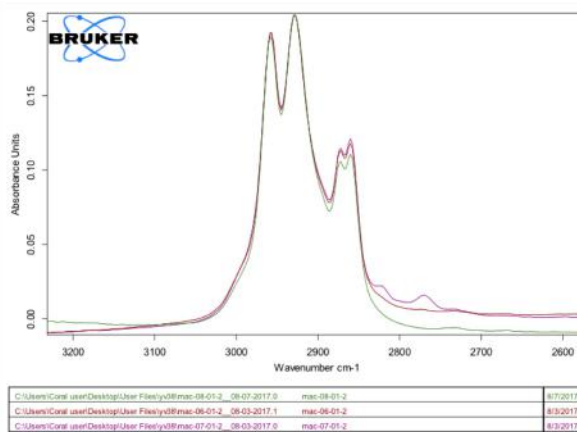


Figure 9. ATR-FTIR of 10% basic (green), 10% acidic (pink), and 10% tri-copolymer (red) showing the disappearance of the amine peak at 2770 and 2810cm⁻¹.

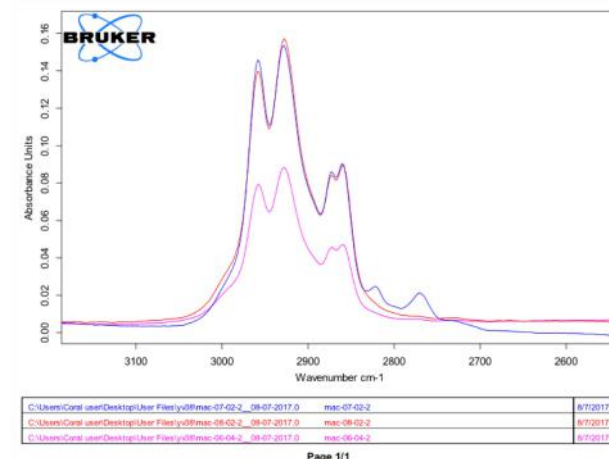


Figure 10. ATR-FTIR of 20% basic (blue), 20% acidic (red), and 40% tri-copolymer (pink) showing the disappearance of the amine peak at 2770 and 2810cm⁻¹.

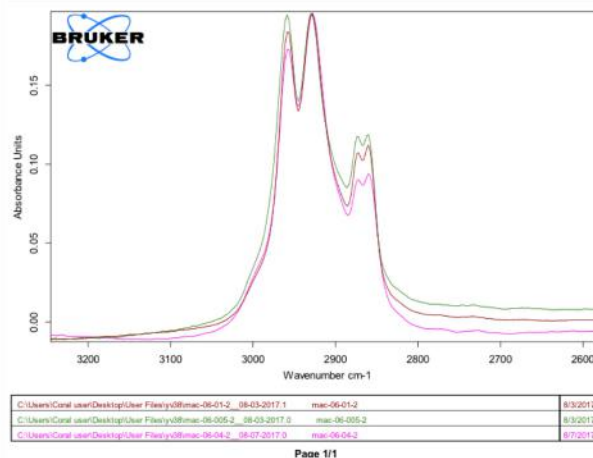


Figure 11. ATR-FTIR of 5% (green), 10% (red), and 40% (pink) tri-copolymer illustrating a decrease in the peaks corresponding to the hydrophobic monomer.

cross-linking agent is a successful synthetic method. With incorporation of higher concentrations of acidic and basic moieties in the tri-copolymer came an undesirable increase in stiffness; the 10, 20, and 40% charged materials were untestable in tension. This increased stiffness supports the claim of successful synthesis as increased ionic cross-linking would increase modulus. However, these materials should be evaluated with tensile testing to quantify the increase in modulus. Use of a more flexible backbone would facilitate the testing and use of similar materials for antifouling purposes.

There are a number of factors to consider going forward with contact angle analysis of these materials. Surface roughness and porosity play a role in contact angle measurements. Though light mineral oil has no chemical interaction with the polymer surfaces, it is important to consider the solubility of the test liquid in the substrate. Absorption testing should be completed before continuing with this test liquid. Further still, use of n-hexadecane or other nonpolar test liquids should be evaluated to find a measurable range of contact angles. Test liquids with known surface energies are preferred for eventual calculation of the surface energy of our material. Owens-Went theory utilizes two test liquids with known surface energies and their measured contact angles with an unknown substrate to evaluate the surface energy of the substrate [8]. This would allow for ease of comparison to known antifouling coatings, such as PDMS, and provide a target behavior for our materials. Ideally, the hydrophobic state of our material would possess a surface energy equivalent to the dispersive component of water; approximately 22 mN/m. This would minimize the time and energy for water to rewet a surface thus prevent protein adhesion [6]. Movement from such a surface energy to a higher surface energy would provide considerable contrast for those fouling organisms able to establish on the hydrophobic surface.

Acknowledgements:

This work was facilitated by Dr. Meredith Silberstein, Department of Mechanical Engineering at Cornell University with mentorship from Yuval Vidavsky.

This work was supported by the Cornell Center for Materials Research with funding from the Research Experience for Undergraduates program (DMR-1460428 and DMR-1120296).

This work made use of the Cornell Center for Materials Research Shared Facilities which are supported through the NSF MRSEC program (DMR-1120296) and the Center for Nanomaterials Engineering & Technology.

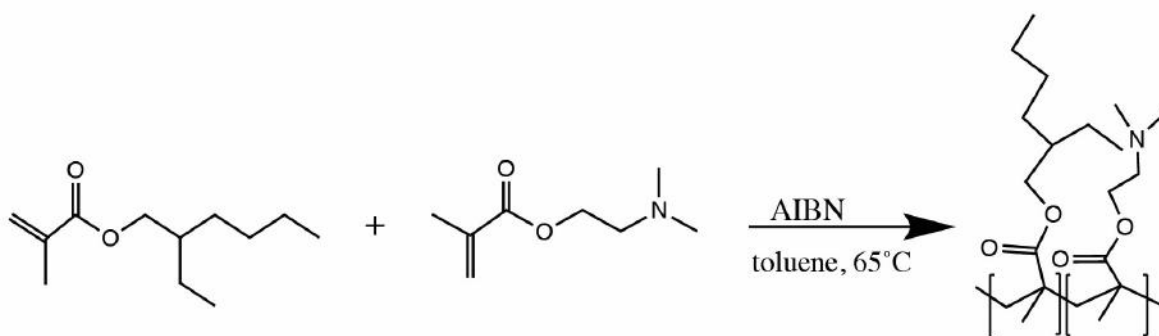
References

- [1] Callow, J. and Callow, M. (2011). Trends in the development of environmentally friendly fouling-resistant marine coatings. *Nature Communications*, 2, p.244.
- [2] M. P. Schultz, J. A. Bendick, E. R. Holm & W. M. Hertel (2011) Economic impact of biofouling on a naval surface ship, *Biofouling*, 27:1, 87-98, DOI: 10.1080/08927014.2010.542809
- [3] Randall S Alberte, Stephen Snyder, Bernard J Zahuranec & Marc Whetstone (1992) Biofouling research needs for the United States Navy: Program history and goals, *Biofouling*, 6:2, 91-95, DOI: 10.1080/08927019209386214
- [4] Feng, S., Wang, Q., Gao, Y., Huang, Y. and Qing, F. (2009). Synthesis and characterization of a novel amphiphilic copolymer capable as anti-biofouling coating material. *Journal of Applied Polymer Science*, 114(4), pp.2071-2078.
- [5] Abraham Marmur (2006) Superhydrophobicity fundamentals: implications to biofouling prevention, *Biofouling*, 22:02, 107-115, DOI: 10.1080/08927010600562328
- [6] Magin, C., Cooper, S. and Brennan, A. (2010). Non-toxic antifouling strategies. *Materials Today*, 13(4), pp.36-44.

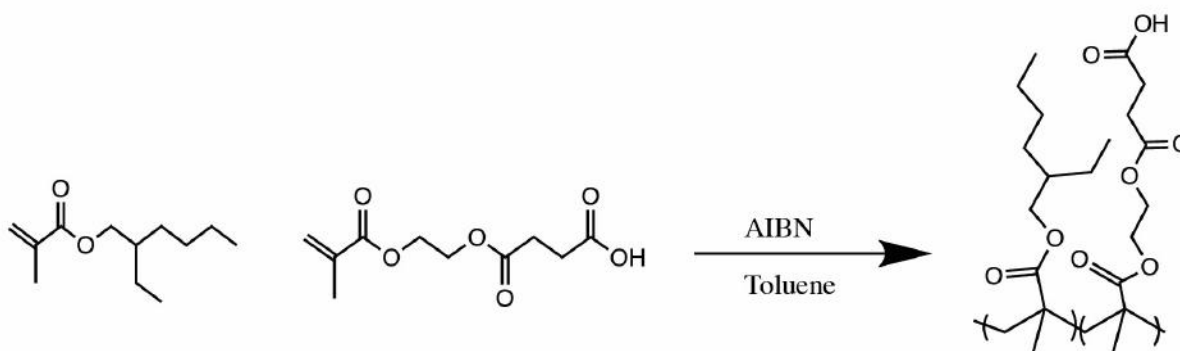
[7] Teo, L., Chen, C. and Kuo, J. (1997). Fourier Transform Infrared Spectroscopy Study on Effects of Temperature on Hydrogen Bonding in Amine-Containing Polyurethanes and Poly(urethane-urea)s.

[8] Rudawska, A. and Jacniacka, E. (2009). Analysis for determining surface free energy uncertainty by the Owen-Wendt method. *International Journal of Adhesion and Adhesives*, 29(4), pp.451-457.

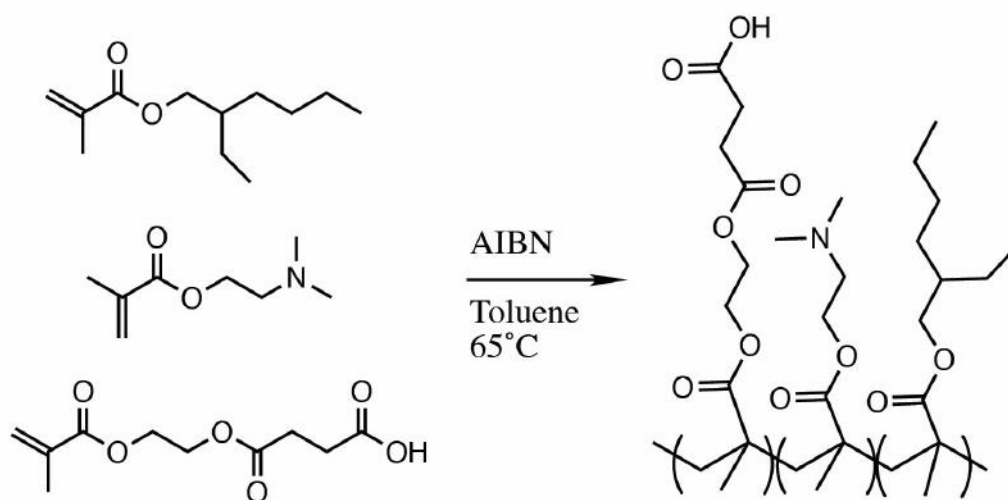
Appendix A: Synthetic Structures



Reaction 1: Synthesis of basic polymer from hydrophobic and amine monomers.

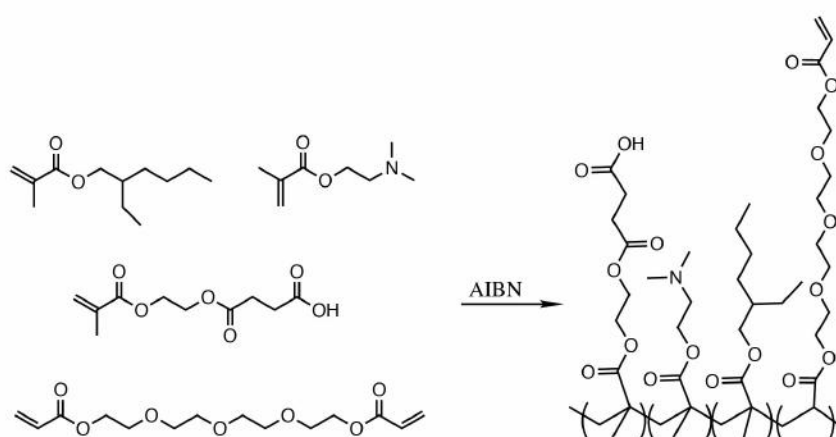


Reaction 2: Synthesis of acidic polymer from hydrophobic and carboxylate monomers.

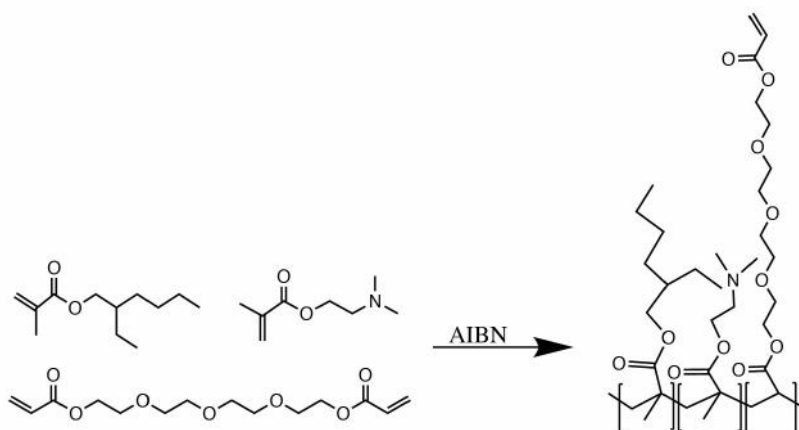


Reaction 3: Synthesis of tri-copolymer from hydrophobic monomer, amine monomer, and carboxylic monomer.

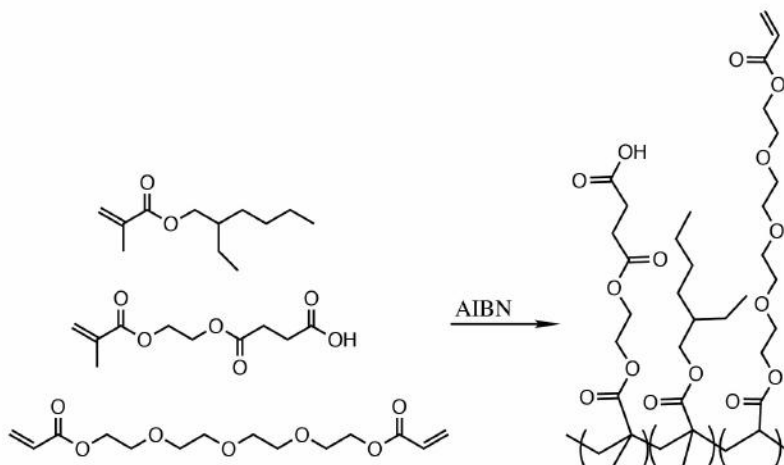
Appendix B: Bulk Polymerization Structures



Appendix B.1. Bulk synthesis of tri-copolymer from acidic, basic, and hydrophobic monomers as well as 1% cross-linking agent.



Appendix B.2. Bulk synthesis of basic polymer with 1% cross-linking agent.



Appendix B.3. Bulk synthesis of acidic polymer with 1% cross-linking agent.

Appendix C:

Swelling of 'thermoplastic' polymers in ethyl acetate from left to right are 10% acid, 5% acid, 5% base, 20% base, 20% acid. Note the lumpy and inhomogeneous texture in each vial.

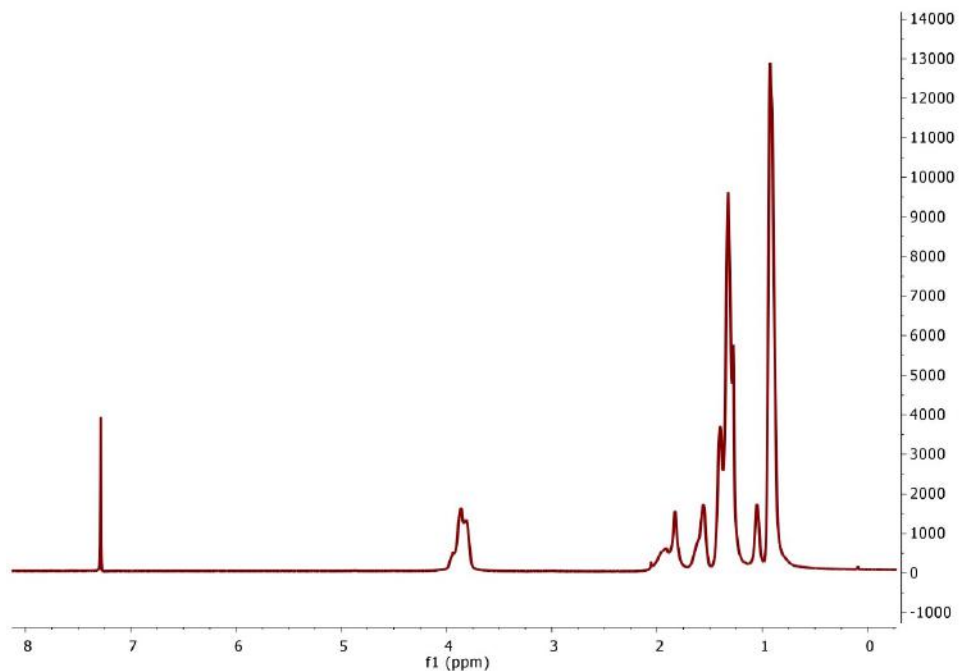


Appendix D:

Photographs of cross-linked materials produced from the thermoplastic synthesis method. From left to right: 10% tri-copolymer, 5% acid, 10% tri-copolymer (top), and 20% tri-copolymer (bottom). Polymer samples failed to spread to fill either the rectangular PDMS molds or circular teflon molds.

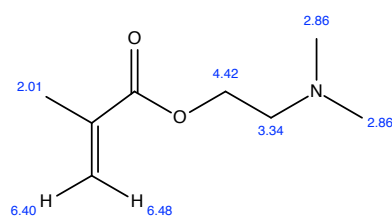


Appendix E:

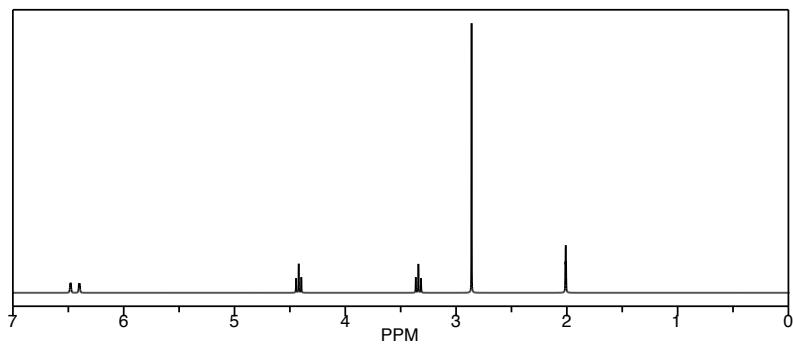


Appendix E.1. ATR-FTIR of 20% acid via hydrolysis. No acid peaks are seen and the peak associated with the hydrophobic monomer has not decreased.

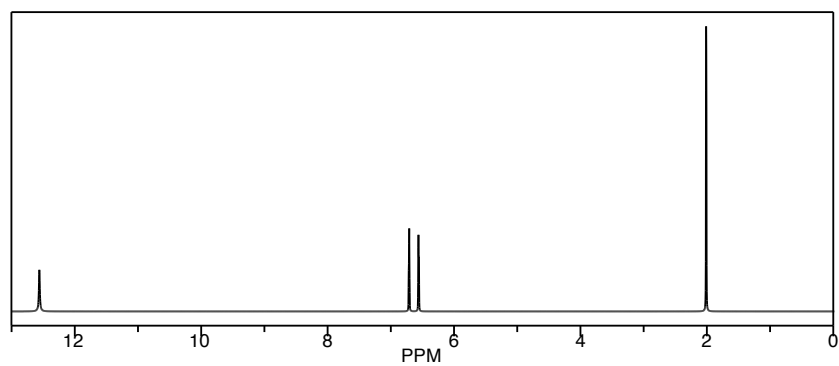
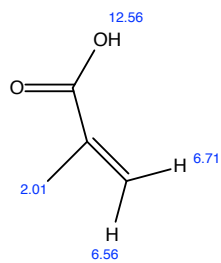
ChemNMR ¹H Estimation



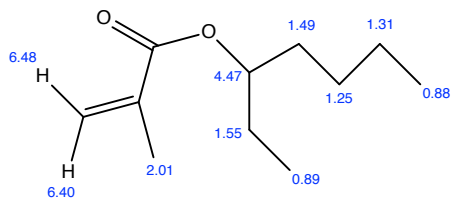
Estimation quality is indicated by color: good, medium, rough



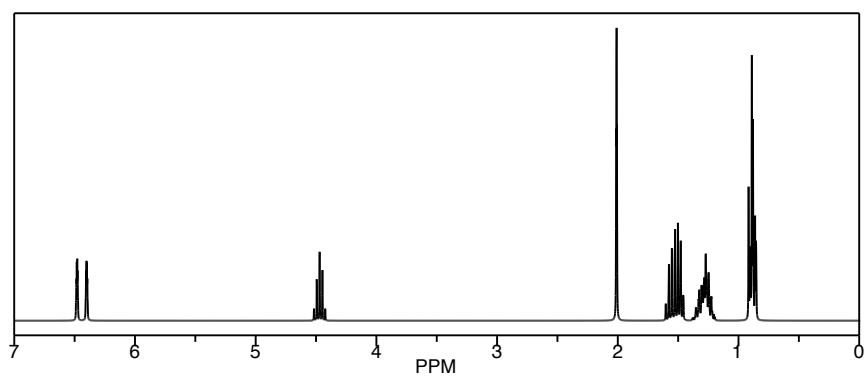
ChemNMR ^1H Estimation



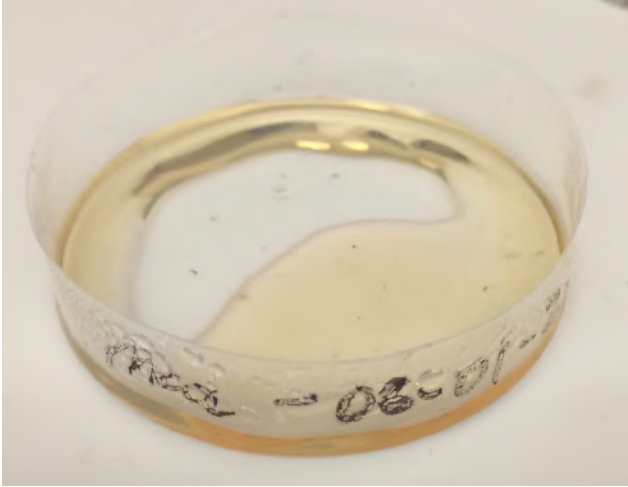
ChemNMR ^1H Estimation



Estimation quality is indicated by color: **good**, **medium**, **rough**



Appendix F



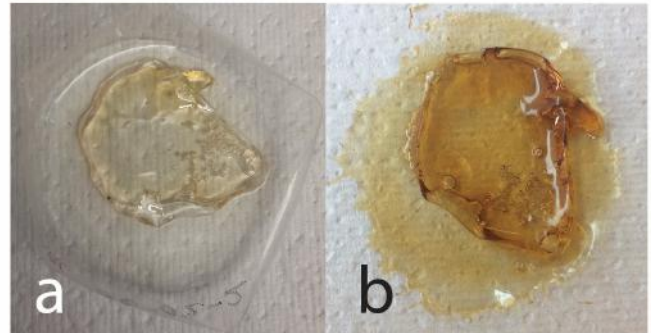
Appendix F.1. Photograph of bulk polymerized polymer processed in the presence of oxygen. Mixture turned yellow-orange in color and evaporated over 10 hours without a visible change in viscosity.



Appendix F.2. Photograph of PDMS mold after polymerization of low viscosity bulk polymer overnight. Polymer was cast to slightly overfill the mold then covered with a piece of acetate to create an anaerobic environment. The white substance infiltrating the PDMS on the right is polymer species that migrated into the substrate.

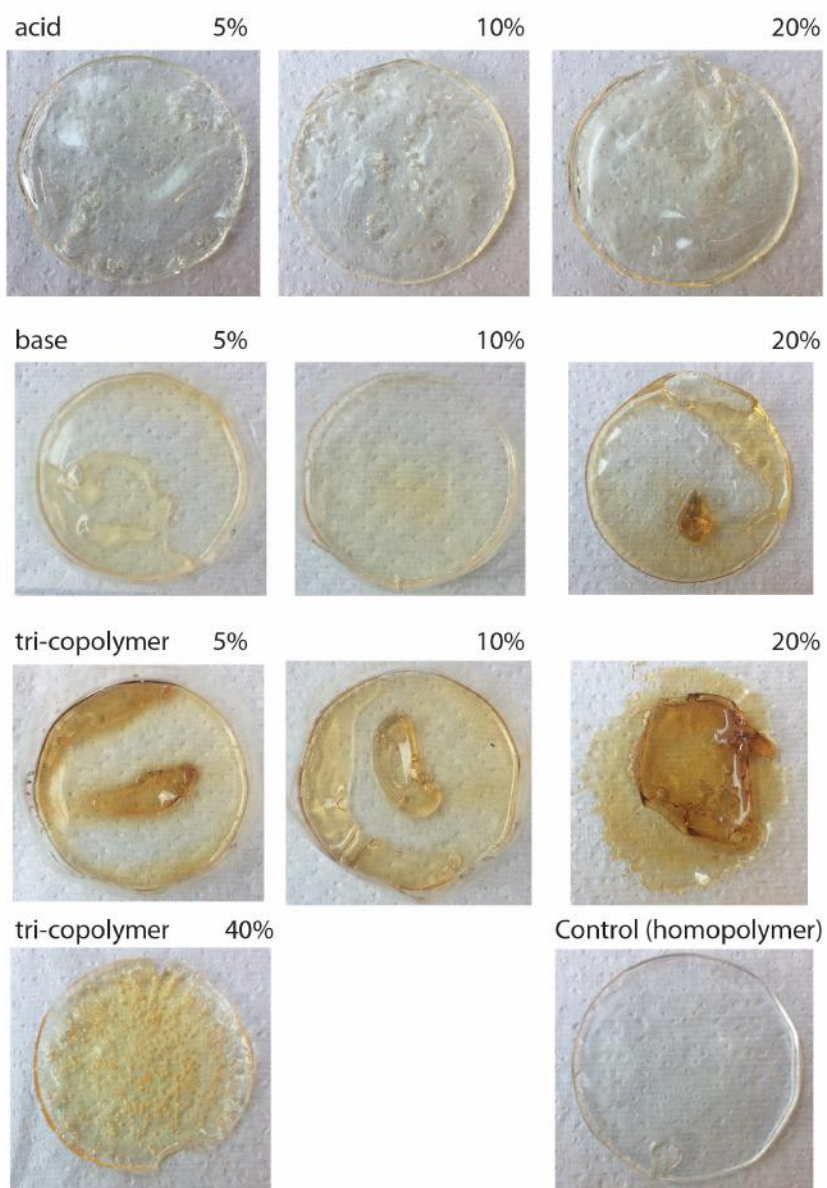


Appendix F.3. Photograph of vials containing bulk synthesis polymers prior to increased viscosity. From left to right the materials are 10% tri-copolymer, 5% tri-copolymer, and 20% basic polymer. The 5% tri-copolymer and 20% basic polymer have rose and yellow-orange colors respectively.



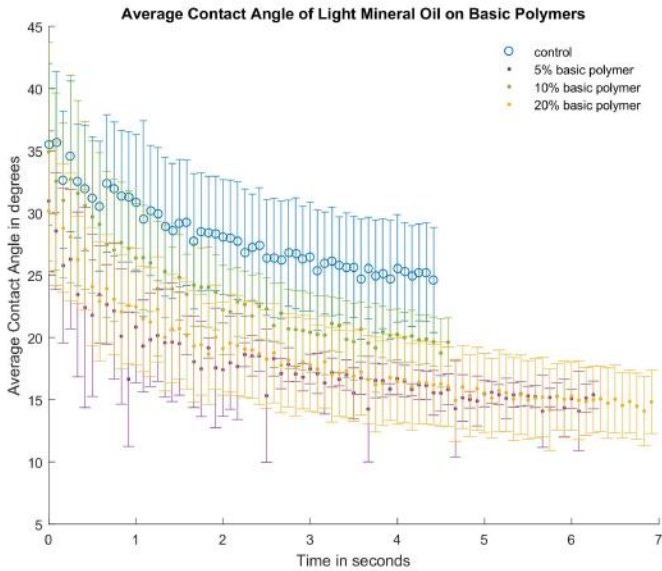
Appendix F.4. Photographs of bulk synthesis 20% tri-copolymer before drying (a) and after drying (b) when a strong gold-orange color appears.

Appendix G

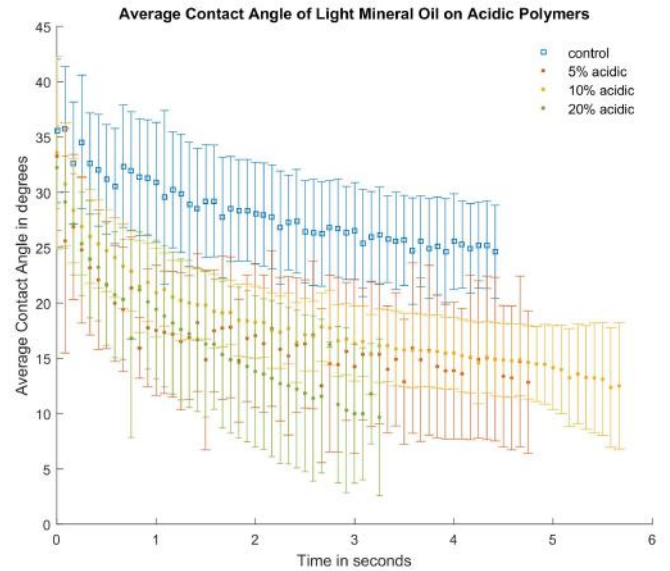


Photographs of all the finished bulk synthesis polymers after drying. The tri-copolymers (5%-20%) and basic polymers (5% and 20%) exhibit rafting due to shrinking of the cross-linked material.

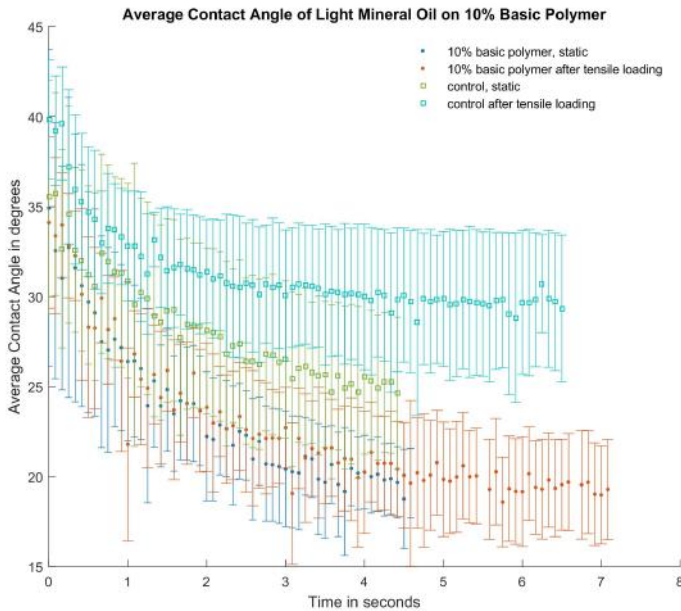
Appendix H



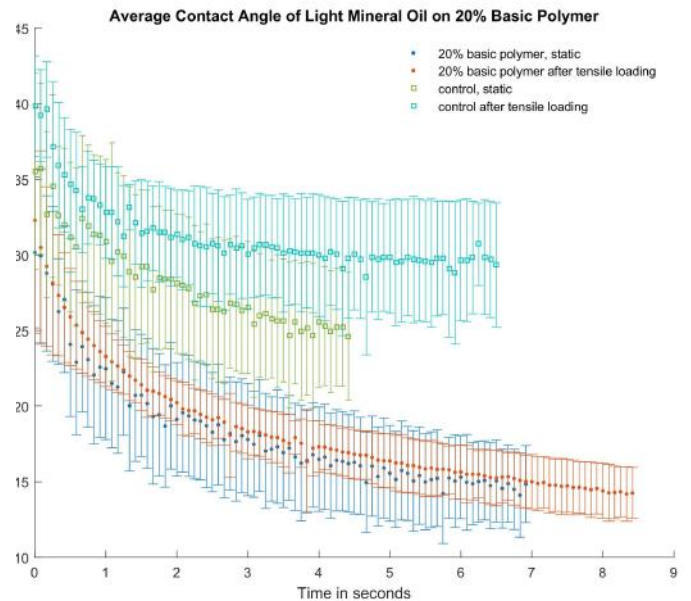
Appendix H.1. The average contact angle of light mineral oil on bulk synthesized basic polymers in a static state. All curves overlap with one another and/or the control.



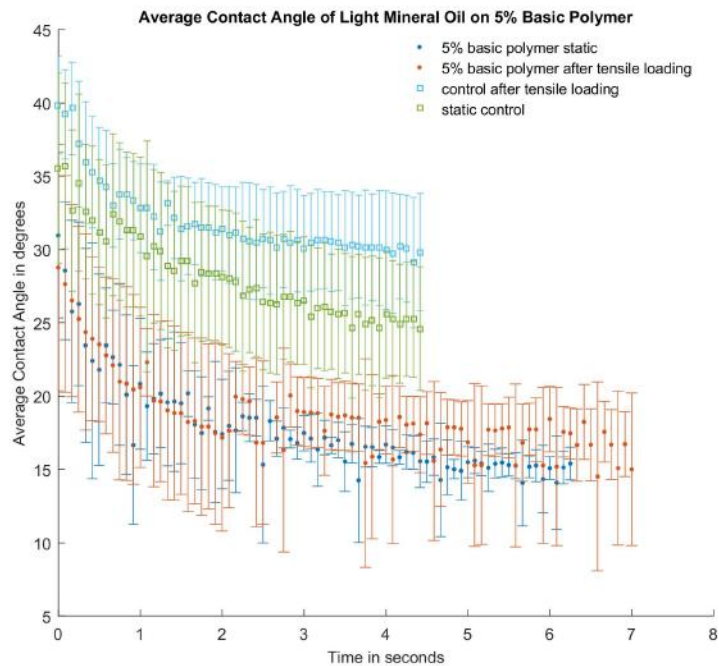
Appendix H.2. The average contact angle of light mineral oil on bulk synthesized acidic polymers in a static state. All curves overlap with one another and/or the control. The 20% acid is noted to decline in contact angle at the greatest rate. However, the change is not great enough to draw conclusions.



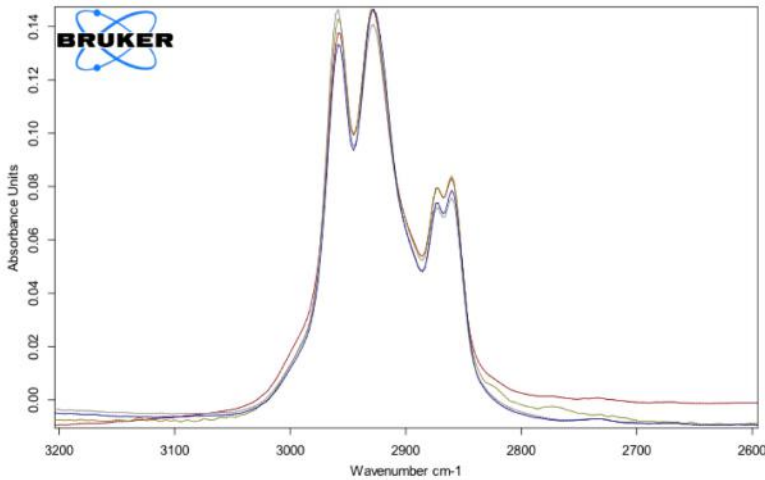
Appendix H.3. The average contact angle of light mineral oil on 10% basic polymer before and after strain compared to the control (EHMA). The static and strain state curves for the 10% basic polymer overlap significantly with one another and upon normalization overlap significantly with the control.



Appendix H.4. The average contact angle of light mineral oil on 20% basic polymer before and after strain compared to the control (EHMA). The static and strain state curves for the 20% basic polymer overlap significantly with one another. Upon normalization, the acid curve does not vary significantly from the control.



Appendix H.5. The average contact angle of light mineral oil on 5% basic polymer before and after strain compared to the control (EHMA). The static and strain state curves for the 5% basic polymer over lap with one another. Upon normalization, the acid curve does not vary significantly from the control.



Appendix H.6. ATR-FTIR spectra of EHMA (blue), 5% acid (green), 5% base (grey), and 10% tri-copolymer. The curves are nearly identical supporting the similarity between the strained contact angle data for the tri-copolymer and control.

C:\Users\Coral_user\Desktop\User Files\y98\mac-012-1-1_08-07-2017.0	mac-012-1-1	8/7/2017
C:\Users\Coral_user\Desktop\User Files\y98\mac-08-005-2_08-07-2017.0	mac-08-005-2	8/7/2017
C:\Users\Coral_user\Desktop\User Files\y98\mac-07-009-2_08-03-2017.0	mac-07-009-2	8/3/2017
C:\Users\Coral_user\Desktop\User Files\y98\mac-06-01-2_08-03-2017.1	mac-06-01-2	8/3/2017

Engineering Band Gap and Electronic Transport in Inorganic Halide Perovskites Through Substitutional Halide Defects

Philippe David,^{*,†} Henry Herbol,[‡] and Paulette Clancy[¶]

[†]*Department of Chemistry, University of Utah, Salt Lake City, Utah 84106, United States*

[‡]*Department of Materials Science and Engineering, Cornell University, Ithaca, New York
14853, United States*

[¶]*Robert F. Smith School of Chemical and Biomolecular Engineering, Cornell University,
Ithaca, New York 14853, United States*

E-mail: philippe.david@utah.edu

Phone: 801 651-2730

Abstract

Organo-metal halide perovskites have been a source of intense interest for their excellent material properties for high efficiency photovoltaics. However, the role of chlorine doping in (Cs/CH₃NH₃)PbI₃ represents an important open issue in the use of hybrid perovskites for photovoltaic applications. Experimental studies have shown that methylammonium lead iodide perovskites doped with chlorine exhibit superior performance with respect to pure MAPbI₃ materials. In this work we report the results of *ab initio* density functional theory and semi-classical Boltzmann transport theory to investigate the effects that novel halide substitutional defects have on the band gap and electronic transport properties.

Introduction

Hybrid lead halide perovskites have been revolutionizing the landscape of emerging photovoltaic technologies. From their first application in 2009 by Kojima et al.¹ as solar cell sensitizers, perovskites have dominated the emerging solar field.²⁻⁴ Because of the rapid growth of efficiency from 3.8% to 22.1% in recent years, perovskite solar cells have drawn significant attention of researchers from both academia and industry.^{2,5-8} Inorganic materials with the perovskites structure have typically had single octahedral cation structure with the formula AMX_3 , where A and M represent inorganic or organic cations and X halide anions. More specifically, they have stoichiometry of AMX_3 where X is an oxide or halide anion such as Cl, Br and I. M refers to a metal cation with a coordination number of 6. The MX_6 octahedral share corners and A is usually a large cation that fills the cub octahedral holes with coordination number of 12. A can be Ca, K, Na, Pb, Sr, or other rare metals. Recently however, double and even tripe perovskites have been proposed as potential environmentally friendly alternatives to the prototypical ABX_3 .^{9,10}

Perovskites have been proposed to be an inexpensive base materials for high-efficiency solar voltaic cells.¹¹ The high power conversion efficiencies of these perovskite solar cells now rival those of traditional silicon-based solar cells. Unlike silicon, perovskites can be processed directly from solution, leading to low-cost and energy-efficient fabrication.¹² The facile low temperature solution-based fabrication of perovskites have made them a leader in energy efficient clean tech material development.¹³ Perovskites also benefit from the fact that they can be manufactured using earth abundant materials unlike many multi-junction solar cells.⁴ The high absorption coefficient, high diffusion length, and high charge-carrier mobilities additionally make perovskites a prime candidate to be replace traditional crystalline silicon photovoltaic cells in the future.¹⁴⁻¹⁶ However, the stability of perovskite solar cells remain a major challenge. Preventing this degradation and determining strategies to improve the long term stability of perovskite solar cells is a major area of focus in the scientific community.^{6,17-19} One way that has been proposed to combat these issues has been

to incorporate a mixture of halides in the perovskite solar cells.²⁰ A number of studies have shown major improvement to charge transfer properties and stability in mixed halide perovskites compared to their single halide counterparts.^{21–25} Thermodynamic arguments have been made that it should be difficult to incorporate a large amount of chlorine inside a lead iodide perovskite.²⁶ Nonetheless, contrary experimental results have shown successful perovskites with the $\text{MAPbI}_{3-x}\text{Cl}_x$ stoichiometry.^{27,28} *ab initio* calculations have shown that carrier relaxation time can be considerably increased by mixing halogen atoms in the perovskite materials.^{21,29,30} These findings all establish the importance of understanding the charge carrier properties of perovskites.^{31,32}

We considered supercells of $\text{CsPb}(\text{I}_x(\text{Cl}/\text{Br})_{1-x})_3$ containing 40 atoms, corresponding to $2 \times 2 \times 2$ unit cells. CsPbI_3 was chosen because of its desirable bandgap of 1.73 eV and the many reports suggesting that mixing halides resulted in improved optical and thermal stability.^{7,33} The material suffers from transitions to a yellow, insulating, non-perovskite phase called the δ -phase at temperatures below 315 C.^{6,17,34} Though some previous work has been done examining this, only two defect structures were examined with very high levels of doping.²⁴ Our work aims to present a more comprehensive picture with a wider range of doping levels and configurations. In this study, a number of defect configurations were generated and relaxed in their pseudo-cubic perovskite structure to try to address the lack of knowledge regarding the possible impact on charge carrier performance of mixed halide systems.³⁵

Methods

We use periodic Density Functional Theory (DFT) to obtain energy-minimized structures and the band diagrams of defects in CsPbI_3 . All DFT calculations in this study were performed using the Quantum Espresso package using the Perdew-Burke-Ernzerhof (PBE) parametrization of the generalized gradient approximation (GGA) as the exchange-correlation

functional.^{36,37} The electron-ionic core interactions were represented using the GBRV ultra-soft pseudopotentials.³⁸ A large 40 Ry kinetic energy cutoff was used for the wavefunctions and a 400 Ry kinetic energy cutoff for the charge density and potential. A $4 \times 4 \times 4$ MonkhorstPack grid was chosen for sampling the Brillouin zone during relaxation and self consistent procedure. All the unit-cell vectors and atom coordinates were relaxed to have Hellmann-Feynman forces lower than $1\text{E-}4$ eV/ \AA and the energy convergence criterion was set to $10\text{E-}5$ eV. Structural optimization was performed with the Broyden-Fletcher-Goldfarb-Shanno quasi-Newton method.

The calculation of transport coefficients using Boltzmann transport theory was done using the BoltzTraP code.³⁹ A $10 \times 10 \times 10$ Monkhorst-Pack k-point mesh was used to calculate the band structure. A dense k-point mesh is necessary because semi-classic transport coefficients are dependent on a smoothed Fourier interpolation of the bands. The basis of this semi-classical Boltzmann theory within the constant relaxation time approximation relies on extracting the α component of the charge carrier group velocity at a band-energies ϵ_i and k-point vector \mathbf{k}

$$v_\alpha(i, \mathbf{k}) = \frac{1}{\hbar} \frac{\partial \epsilon_{i,\mathbf{k}}}{\partial k_\alpha} \quad (1)$$

The conductivity tensors can thus be derived

$$\sigma_{\alpha\beta}(i, \mathbf{k}) = e^2 \tau_{i,\mathbf{k}} v_\alpha(i, \mathbf{k}) v_\beta(i, \mathbf{k}) \quad (2)$$

where τ is the relaxation time and e is elementary charge. The relaxation time, dependent on both the band energy and the \mathbf{k} vector direction, is assumed to be constant. Through the integration of the conductivity distributions, Eq (2), the transport tensors as a function of the temperature, T , and chemical potential μ can then be calculated by

$$\sigma_{\alpha\beta}(T; \mu) = \frac{1}{\Omega} \int \sigma_{\alpha\beta}(\epsilon) \left[-\frac{\partial f_\mu(T; \epsilon)}{\partial \epsilon} \right] d\epsilon \quad (3)$$

$$v_{\alpha\beta}(T; \mu) = \frac{1}{eT\Omega} \int \sigma_{\alpha\beta}(\epsilon)(\epsilon - \mu) \left[-\frac{\partial f_{\mu}(T; \epsilon)}{\partial \epsilon} \right] d\epsilon \quad (4)$$

$$\kappa_{\alpha\beta}(T; \mu) = \frac{1}{e^2 T \Omega} \int \sigma_{\alpha\beta}(\epsilon)(\epsilon - \mu)^2 \left[-\frac{\partial f_{\mu}(T; \epsilon)}{\partial \epsilon} \right] d\epsilon \quad (5)$$

With Eq. (4), the Seebeck coefficient can be calculated

$$S_{ij} = E_i(\Delta_j T)^{-1} = (\sigma^{-1})_{\alpha i} v_{\alpha j} \quad (6)$$

While Eq. (3) is in principle exact within the semiclassical theory, analytical solutions of the Boltzmann equation are possible only under very restrictive assumptions. In this work, the relaxation time and local thermal equilibrium approximations are invoked. In the first approximation, τ the microscopic relaxation time, is considered to be constant and thermally and directionally independent. The local thermal equilibrium approximation simply states that the band structure temperature dependence is not taken into account. This method has been used in many previous works to determine the semi-classic transport coefficients.^{19,39–42}

Results and discussion

A. Structural Properties and Band Gap Variation

In our study of defect properties, all calculations used super cells of 40 atoms corresponding to $2 \times 2 \times 2$ unit cells. In addition to the perfect CsPbI₃ perovskite, nine defect structures were examined with both chlorine and bromine incorporated in the iodide-based structure. Each of the nine structures corresponded to different doping levels and defect configurations. These structures in order of increasing doping concentration are described in detail in the following paragraph: The structure with the lowest doping concentration was a single point defect (1 chloride/bromide:23 iodide atoms). The incorporation of this defect caused a

slight contraction in a single lattice dimension. Additionally, three structures with 2 point defects (2 chloride/bromide:22 iodide atoms) placed inside were also examined in this work. One of the structures corresponded to two defects placed in non-adjacent locations. This structure was found by generating 10 random 2 point non-adjacent defect configurations and by selecting the lowest energy structure after relaxation. The other two corresponded to placing the two defect halides adjacent to each other in a lattice plane. These can be described as a sort of 2-dimensional line defect with one of the systems having a Pb atom in between them and the other being located on the corner edges of a conventional perovskite unit cell. Two structures with 4 point defects (4 chloride/bromide:20 iodide atoms) were generated with one having the four defects together in a plane and the other having them in four random configurations. The random configuration was generated in a similar manner to the non-adjacent 2 point defect system. One structure corresponded to having all the halides that surrounded a single Pb atom being replaced with an alternative halide. This structure resulted in a large amount of disorder when relaxed and is most likely not a very stable system. A structure with an entire plane of iodides being replaced was also examined. Lastly, CsPbI_2X for $\text{X}=\text{Cl}$ and Br employed in a stacked planar architecture was also investigated. The chlorine-doped structures will be the main focus of this work as there were no large differences in the calculated electronic and carrier transport properties between the chlorine and bromine doped systems.

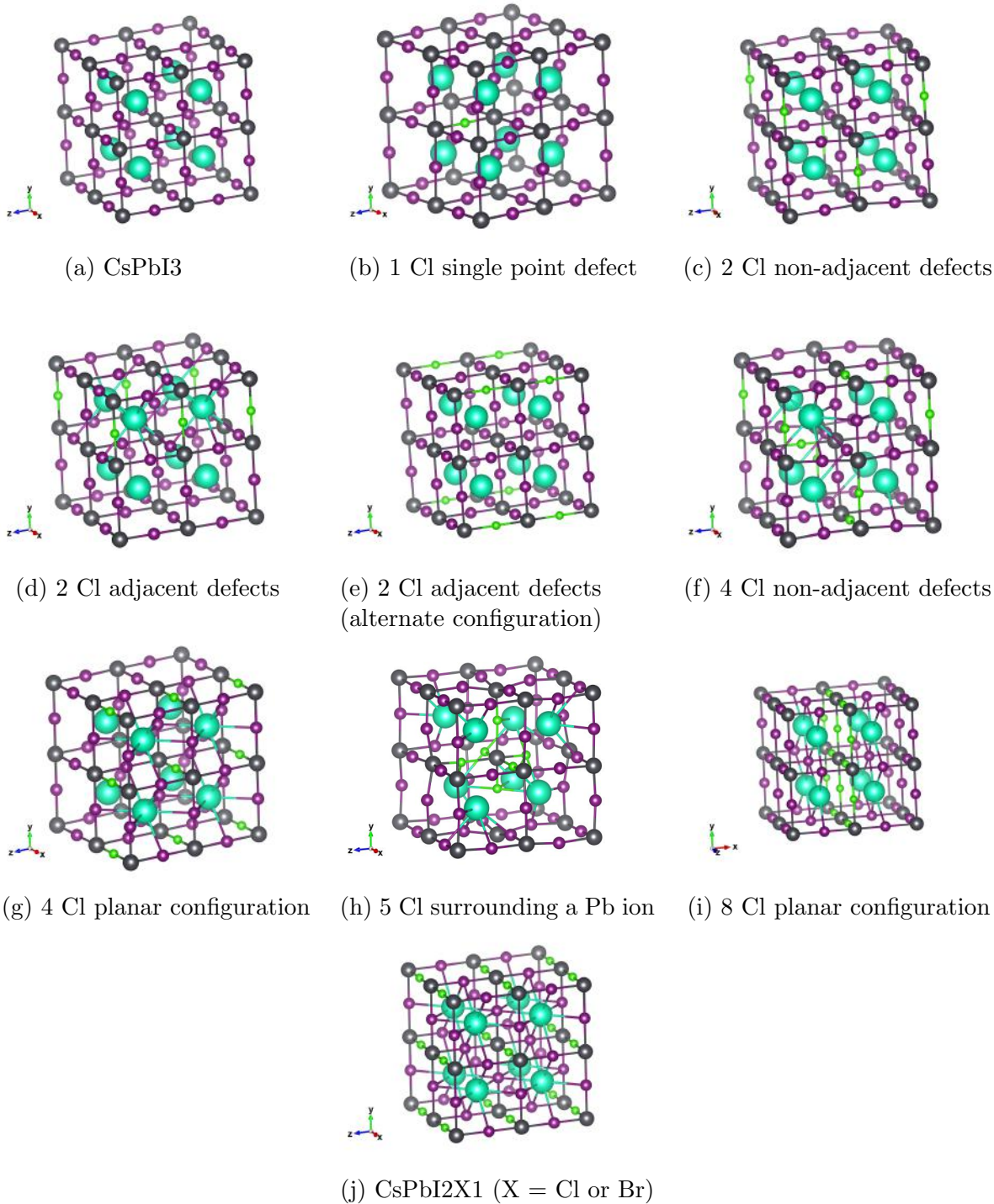


Figure 1: Optimized structures for the considered defect configurations of CsPbI₃. The chlorine, iodide, lead, and cesium atoms are colored in green, purple, grey, and green respectively

Table 1: Lattice constants of considered perovskites.

Structure	a (\AA)	b (\AA)	c (\AA)
CsPbI ₃ (exp)	6.39		
CsPbI ₃ (calc)	6.39		
1 Cl, 1:23 Cl:I	6.39	6.39	6.32
2 Cl, 1:11 Cl:I (random)	6.40	6.24	6.40
2 Cl, 1:11 Cl:I (line)	6.40	6.24	6.40
2 Cl, 1:11 Cl:I (line alt.)	6.39	6.39	6.26
4 Cl, 1:5 Cl:I (random)	6.34	6.24	6.31
4 Cl, 1:5 Cl:I (plane)	6.05	6.41	6.41
5 Cl, 5:19 Cl:I (disordered)	6.34	6.34	6.34
5 Cl, 5:19 Cl:I	1.49		
8 Cl, CsPbI ₂ Cl	5.69	6.43	6.43
8 Cl, CsPbI ₂ Cl (plane)	6.40	6.12	6.12

It should be noted that relaxing the configuration shown in Figure 1 (h) and more in detail in Figure 2 with 5 Cl resulted in a rather distorted geometry in both chlorine and bromine doped structures. This distortion caused a relatively large increase in the band gap. Eliminating this disorder while maintaining the optimized lattice constants nullified the observed increase in bandgap.

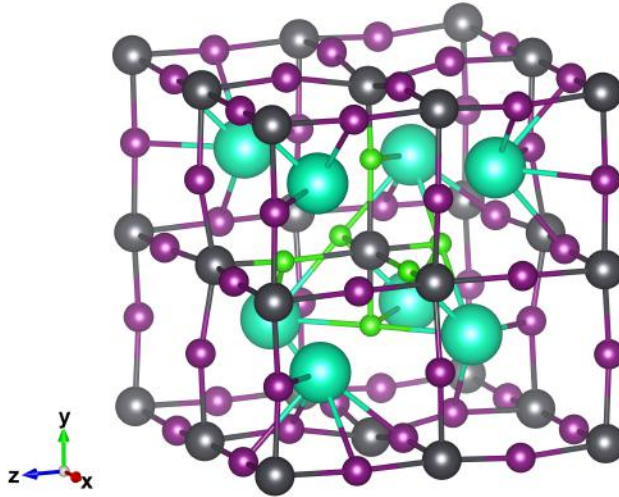


Figure 2: The disordered structure is obvious in the 5 Cl defect structure.

The most intriguing of the investigated defect structures was the 8 Cl planar configuration. The plane of more electronegative chlorine atoms had the interesting effect of drawing the cesium cations closer to the plane. The result of this caused a noticeable reduction in the bandgap. This geometry was not observed to such an extent in the bromine doped structure and calculated band gap in that system was not changed to such an extent.

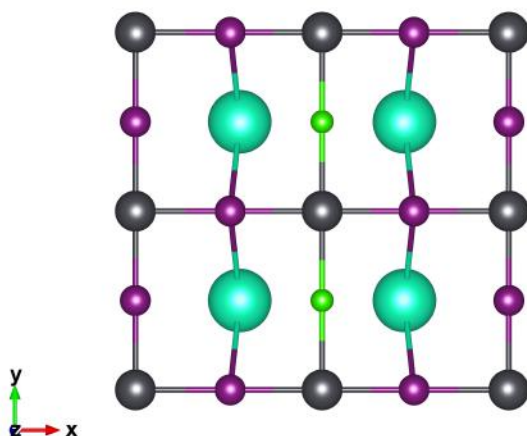
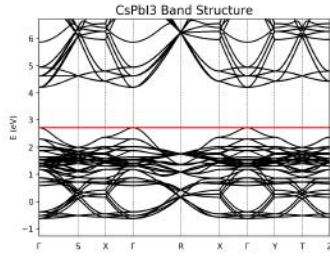
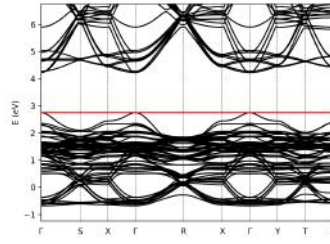


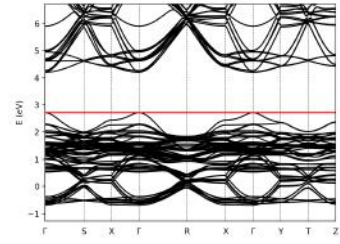
Figure 3: The displacement of the cesium cations toward the plane of chlorines in the optimized structure is obvious from a side view.



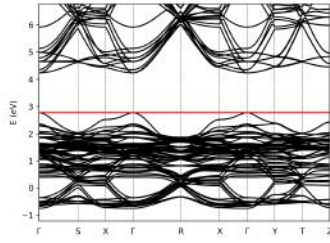
(a) CsPbI₃



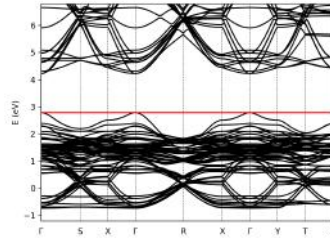
(b) 1 Cl single point defect



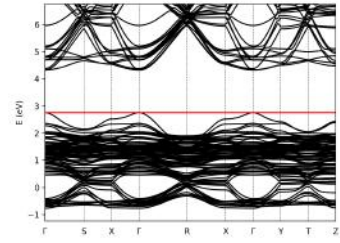
(c) 2 Cl non-adjacent defects



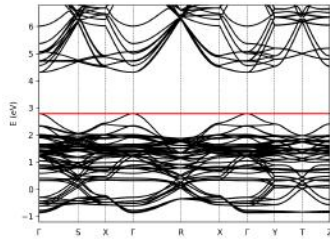
(d) 2 Cl adjacent defects



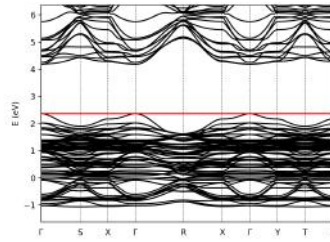
(e) 2 Cl adjacent defects
(alternate configuration)



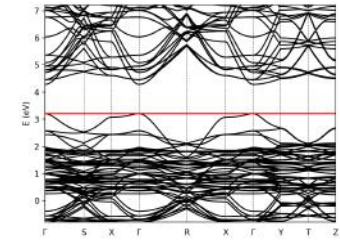
(f) 4 Cl non-adjacent defects



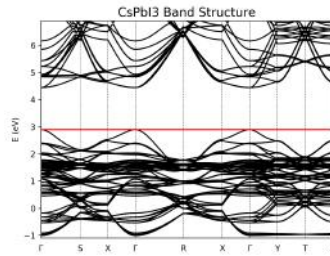
(g) CsPbI₃ (4 Defects in
plane)



(h) CsPbI₃ (5 Defects sur-
rounding a Pb)



(i) 8 Cl planar configuration



(j) CsPbI₂Cl₁ (X = Cl or Br)

Figure 4: Calculated electronic band structures shown in the vicinity of the Fermi level. The Fermi level is shown in red.

The band structures of the considered compounds along the directions Γ -S-X- Γ -R-X- Γ -Y-T-Z of the first BZ are shown in Figure 4. These k-points represent high symmetry points in the $Pmna$ space group. All of the structures have a direct gap at the Γ point. In general, the doped structures did not exhibit any major deviation from the pure lead iodide perovskite except for a single case.³⁰ More analysis is required to explain relatively large decrease in the bandgap for the CsPbI_2Cl planar chlorine defect structure. Examining the partial density of states in the system could elucidate on the origins of the decrease.

Table 2: Calculated bandgaps of considered chlorine doped perovskites.

Structure	E_g (eV)	$E_g(\text{exp})$ (eV)
CsPbI ₃	1.48	1.73 ^{Filip2014}
1 Cl, 1:23 Cl:I	1.47	
2 Cl, 1:11 Cl:I (random)	1.46	
2 Cl, 1:11 Cl:I (line)	1.46	
2 Cl, 1:11 Cl:I (line alt.)	1.44	
4 Cl, 1:5 Cl:I (random)	1.57	
4 Cl, 1:5 Cl:I (plane)	1.52	
5 Cl, 5:19 Cl:I (unit) (disordered)	1.81	
5 Cl, 5:19 Cl:I (unit)	1.49	
8 Cl, CsPbI ₂ Cl	1.55	
8 Cl, CsPbI ₂ Cl (plane)	1.28	

B. Electronic Transport and Thermoelectric Properties

To gain high thermoelectric efficiency, it is necessary that the material possesses high electrical conductivity, a large Seebeck coefficient and low thermal conductivity. In Figure 5, the calculated electrical conductivity (σ/τ) are shown for all the structures. All of the defect structures exhibit lower overall conductivity compared to the pure structure though the difference is relatively minor for most and all the defect systems have conductivities within an order of magnitude of the pure structure. These conductivities were calculated at three different temperatures and very little temperature dependence on the conductivity is seen in any of the systems. The disordered nature of the 5 Cl defect configuration is evident in Figure 5. (h) having the lowest conductivity of all. The reduced conductivity in the doped systems

is not too surprising considering that the defects cause nonradiative recombination, which is very detrimental charge carrier properties. Defects on surfaces or grain boundaries are generally expected to be detrimental to the performance. However, nonadiabatic molecular dynamics combined with ab initio time-domain density functional theory computational work has shown that the doping of lead iodide perovskites with chlorine atoms reduces charge recombination.^{43,44} Thus, there is probably a tradeoff involved.

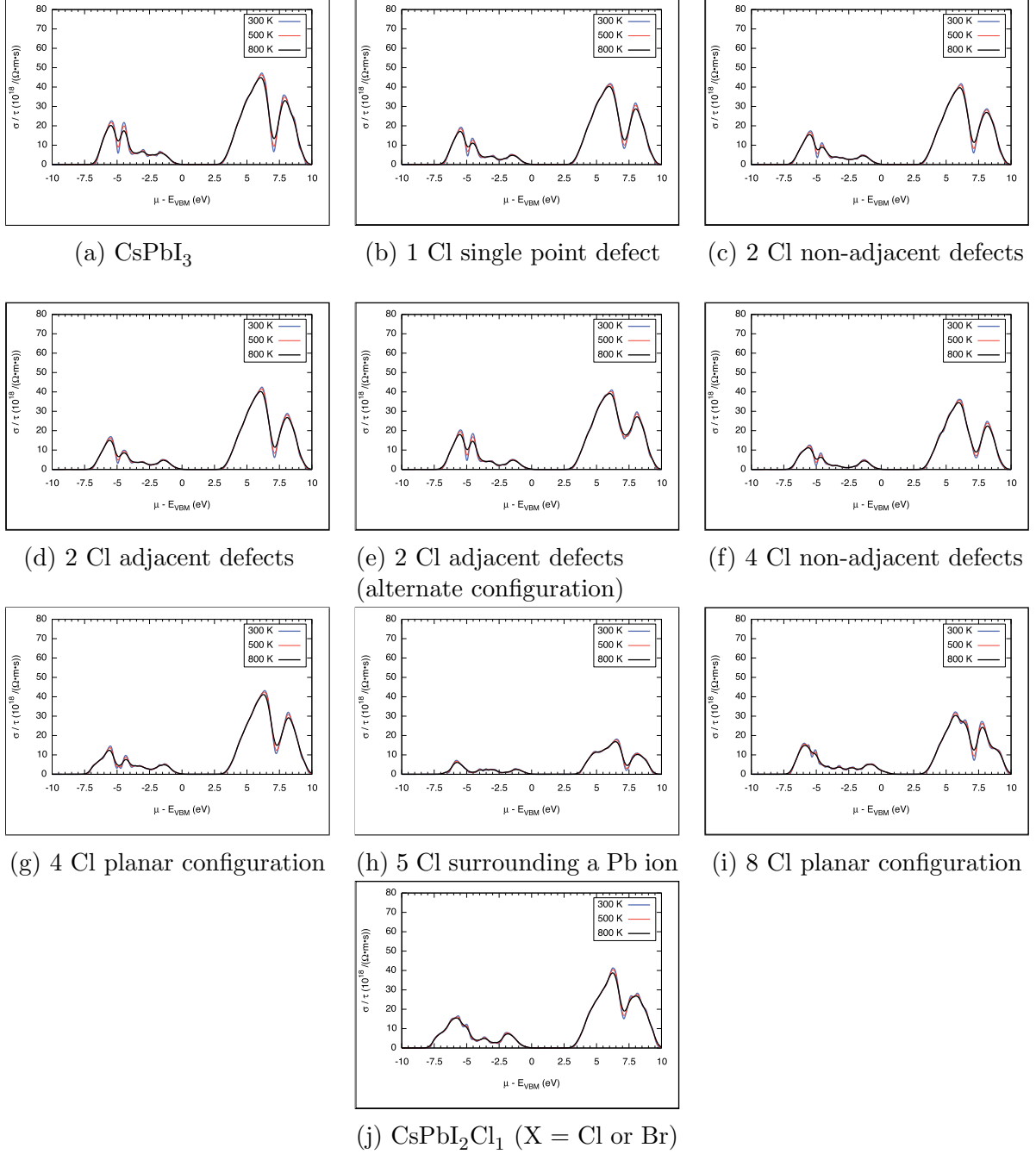


Figure 5: Conductivity per unit relaxation time, σ/τ , as a function of the chemical potential for the optimized defect configurations of CsPbI₃ computed at three different temperatures: 300 K (blue), 500 K (red), and 800 K (black).

In further investigation, the Seebeck coefficient as a function of chemical potential at three constant temperatures (300, 600 and 900 K) has been calculated. The sign of S indicates

the type of dominant charge carriers: S with a positive sign represents the p-type materials, whereas n-type materials have a negative S . Following Figure 6, it is clear that the Seebeck coefficient has a positive sign which indicates p-type conduction at Fermi level in all the structures. The Seebeck coefficient tensors show the directional dependence of S for all the different structures is very minor.

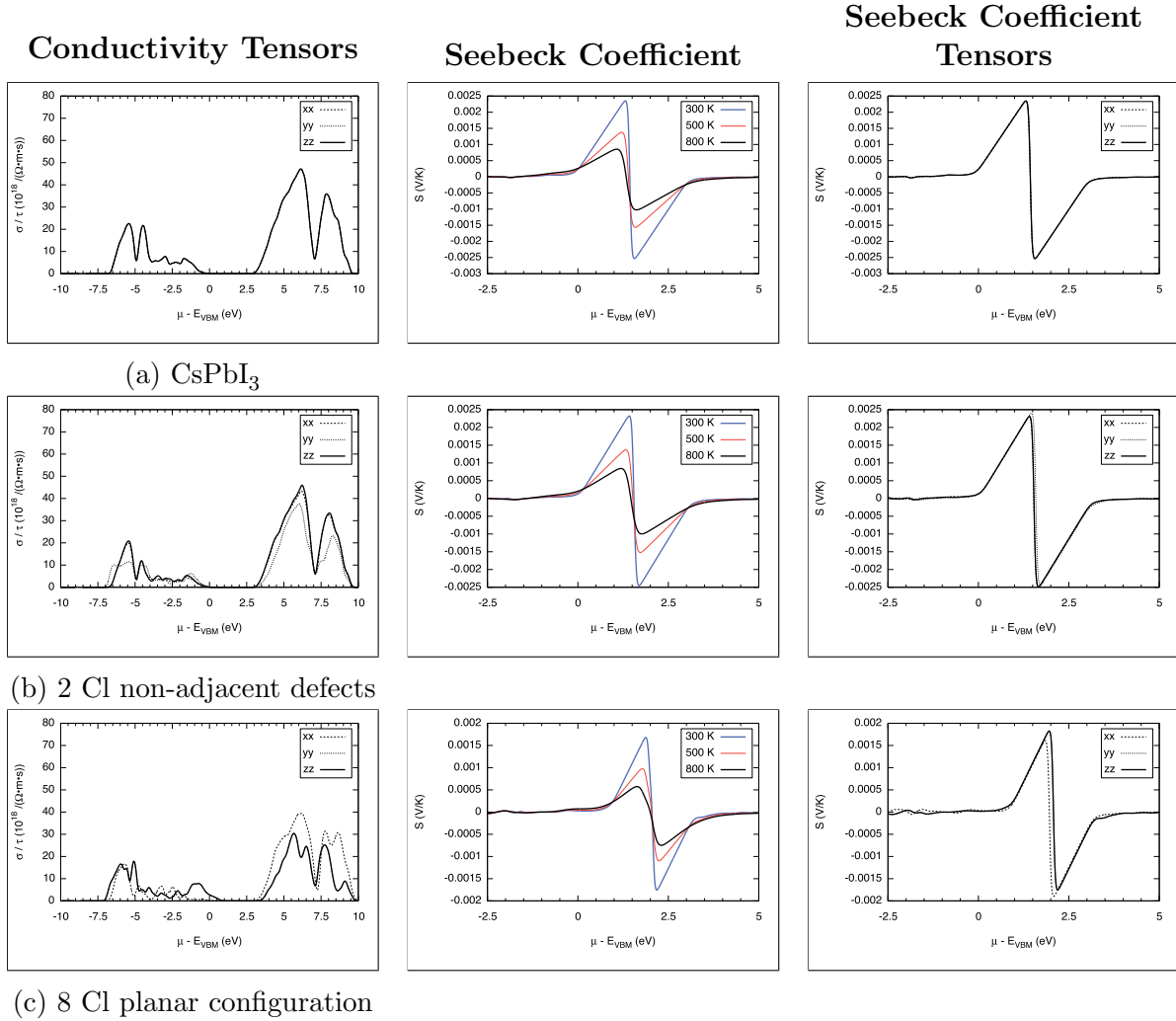


Figure 6: Transport coefficients as a function of chemical potential arranged in three columns. The second column represents the Seebeck coefficient (S). The first and third columns show the conductivity and Seebeck coefficient along the three principal orthogonal directions (x , y and z) for the three structures.

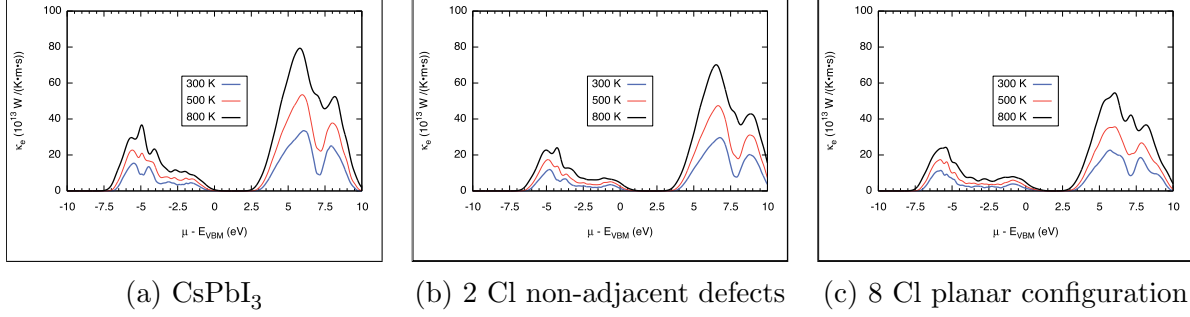


Figure 7: Electron contribution to thermal conductivity (κ_e), with respect to the chemical potential (μ), and at three different temperatures, 300 K (blue), 500 K (red), and 800 K (black).

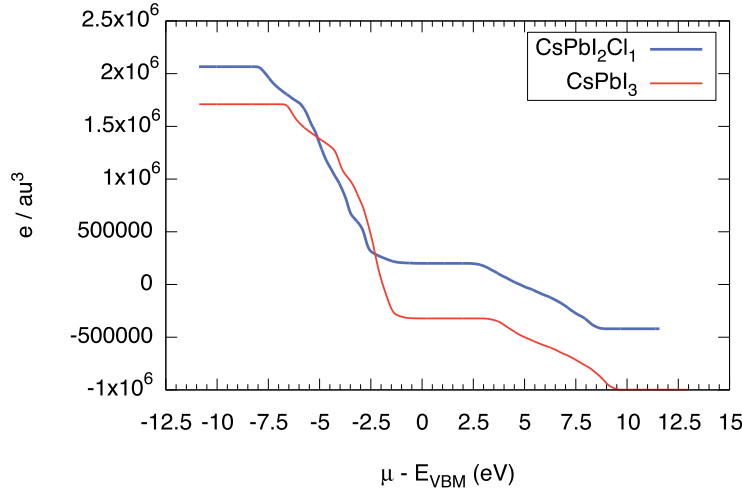


Figure 8: The calculated number of carriers n (density of states) plotted as a function of chemical potential μ for both CsPbI_3 and $\text{CsPbI}_2\text{Cl}_1$ with chlorines in a planar configuration at 300K.

From Boltzmann transport theory, S , κ_e and σ/τ are smaller for all the considered mixed halide structures compared to the value for the pure perovskite. From Figure 8, it is evident that the Cl doped perovskites have more carriers compared to the simple perovskite lattices effecting in a lower S . These results suggest that the excellent charge carrier transportation reported for mixed halide perovskites is not simply due to improment of bulk properties. Some have argued that the increased performance might be due to the role of interfacial chlorine.^{45–48} It has also been proposed that chlorine-mediated production can result in

hysteresis-free and highly stable perovskite solar cells and that the increased crystallinity might be the source of the improved charge carrier values.⁴⁹ This view would align well with the theory that the chlorines play a mostly interfacial role.

Conclusion

In summary, we present via first-principle density functional calculations an exploration of halide substitutional defects in high-performance inorganic perovskites with desired intrinsic photovoltaic functionalities. Our results show that the charge carrier performance of the fully inorganic mixed halide perovskites do not show the drastically improved the charge transport properties that has been demonstrated experimentally.³⁰ It is significant to note that, overall, the influence of chlorine in this performance enchantment remains uncertain. What can be concluded is that the reported increase in carrier transport must be coming from another source.⁴⁵ Additionally, our results confirm previous computational and theoretical work that random doping does not have a major effect on the bandgap. Finally, we propose a possible way for engineering the bandgap through a novel defect superlattice structure.

Acknowledgement

The author thanks Nathan Fox for his helpful discussions on periodic density functional theory. The author also wishes to thank Henry Herbol for his many helpful discussions, mentorship, and guidance on this project. Lastly, the author wishes to profusely thank Professor Paulette Clancy for the opportunity and for all her helpful advice and direction. The author also acknowledges the generous allocation of computer time provided at the Cornell Institute for Computational Science and Engineering (ICSE). This work made use of the Cornell Center for Materials Research Shared Facilities which are supported through the NSF MRSEC program (DMR-1120296). This work was funded by the National Science Foundation (NSF) grant CMMI-0856488. This work was supported by the Cornell Center for

Materials Research with funding from the Research Experience for Undergraduates program (DMR-1460428 and DMR-1120296).

References

- (1) Akihiro Kojima, Kenjiro Teshima, Yasuo Shirai,; Miyasaka, T. *J Am Chem Soc* **2009**, *131*, 6050–6051.
- (2) Yin, W.-J. W. J.; Yang, J.-H. H. J.; Kang, J.; Yan, Y. F.; Wei, S.-H. H. *Journal of Materials Chemistry A* **2015**, *3*, 8926–8942.
- (3) Zhu, K. *Chemical Society Reviews* **2016**, *45*, 655–689.
- (4) Luo, J.; Im, J.-H.; Mayer, M. T.; Schreier, M.; Nazeeruddin, M. K.; Park, N.-G.; Tilley, S. D.; Fan, H. J.; Grätzel, M. *Science* **2014**, *345*, 1593–1596.
- (5) Yang, S.; Fu, W.; Zhang, Z.; Chen, H.; Li, C.-Z. *J. Mater. Chem. A* **2017**, *00*, 1–21.
- (6) Stoumpos, C. C.; Malliakas, C. D.; Peters, J. A.; Liu, Z.; Sebastian, M.; Im, J.; Chasapis, T. C.; Wibowo, A. C.; Chung, D. Y.; Freeman, A. J.; Wessels, B. W.; Kanatzidis, M. G. *Crystal Growth & Design* **2013**, *13*, 27222727.
- (7) Chen, Q.; Zhou, H.; Fang, Y.; Stieg, A. Z.; Song, T.-B.; Wang, H.-H.; Xu, X.; Liu, Y.; Lu, S.; You, J.; Sun, P.; McKay, J.; Goorsky, M. S.; Yang, Y. *Nature Communications* **2015**, *6*, 1–9.
- (8) Stevenson, J.; Sorenson, B.; Subramaniam, V. H.; Raiford, J.; Khlyabich, P. P.; Loo, Y.-l.; Clancy, P. **2017**,
- (9) Forgács, D.; Pérez, D.; Rey, D.; Ávila, J.; Momblona, C.; Gil-Escrig, L.; Dänekamp, B.; Sessolo, M.; Bolink, H. J. *J. Mater. Chem. A* **2016**, *00*, 1–3.

- (10) Volonakis, G.; Haghighirad, A. A.; Milot, R. L.; Sio, W. H.; Filip, M. R.; Wenger, B.; Johnston, M. B.; Herz, L. M.; Snaith, H. J.; Giustino, F. **2017**,
- (11) Shin, S. S.; Yeom, E. J.; Yang, W. S.; Hur, S.; Kim, M. G.; Im, J.; Seo, J.; Noh, J. H.; Seok, S. I. *Science* **2017**, *356*, 167–171.
- (12) Brenner, T. M.; Egger, D. A.; Kronik, L.; Hodes, G.; Cahen, D. *Nature Reviews Materials* **2016**, *1*, 15007.
- (13) Chen, Q.; Zhou, H.; Hong, Z.; Luo, S.; Duan, H.-S.; Wang, H.-H.; Liu, Y.; Li, G.; Yang, Y. *Journal of the American Chemical Society* **2013**, *136*, 622–625.
- (14) Yang, X.; Wang, Y.; Li, H.; Sheng, C. **2016**, 23299–23303.
- (15) Stranks, S. D.; Eperon, G. E.; Grancini, G.; Menelaou, C.; Alcocer, M. J.; Leijtens, T.; Herz, L. M.; Petrozza, A.; Snaith, H. J. *Science* **2013**, *342*, 341–344.
- (16) Xing, G.; Mathews, N.; Sun, S.; Lim, S. S.; Lam, Y. M.; Grätzel, M.; Mhaisalkar, S.; Sum, T. C. *Science* **2013**, *342*, 344–347.
- (17) Stoumpos, C. C.; Malliakas, C. D.; Kanatzidis, M. G. *Inorganic Chemistry* **2013**, *52*, 9019–9038.
- (18) Manser, J. S. *Nature Photonics* **2014**, *8*, 737–743.
- (19) Balasubramanian, G. *Nanoscale* **2017**, *9*, 8600–8607.
- (20) Linaburg, M. R.; McClure, E. T.; Majher, J. D.; Woodward, P. M. **2017**,
- (21) Noh, J. H.; Im, S. H.; Heo, J. H.; Mandal, T. N.; Seok, S. I. *Nano Letters* **2013**, *13*, 1764–1769, PMID: 23517331.
- (22) Stranks, S. D.; Eperon, G. E.; Grancini, G.; Menelaou, C.; Alcocer, M. J. P.; Leijtens, T.; Herz, L. M.; Petrozza, A.; Snaith, H. J. *Science* **2013**, *342*, 341–344.

- (23) Dastidar, S.; Egger, D. A.; Tan, L. Z.; Cromer, S. B.; Dillon, A. D.; Liu, S.; Kronik, L.; Rappe, A. M.; Fafarman, A. T. *Nano Letters* **2016**, *16*, 3563–3570.
- (24) Quarti, C.; Mosconi, E.; Umari, P.; De Angelis, F. *Inorganic Chemistry* **2017**, *56*, 74–83.
- (25) Kiermasch, D.; Rieder, P.; Tvingstedt, K.; Baumann, A.; Dyakonov, V. *Nature Publishing Group* **2016**, 1–7.
- (26) Yin, W.-j.; Yan, Y.; Wei, S.-h. **2014**,
- (27) Liu, M.; Johnston, M. B.; Snaith, H. J. *Nature* **2013**, *501*, 395–398.
- (28) Lee, M. M.; Teuscher, J.; Miyasaka, T.; Murakami, T. N.; Snaith, H. J. *Science* **2012**, *338*, 643–647.
- (29) Madjet, M. E.-A. E.-A.; Akimov, A.; El-Mellouhi, F.; Berdiyurov, G.; Ashhab, S.; Tabet, N.; Kais, S. *Phys. Chem. Chem. Phys.* **2016**, *18*, 5219–5231.
- (30) Colella, S.; Mosconi, E.; Fedeli, P.; Listorti, A.; Gazza, F.; Orlandi, F.; Ferro, P.; Besagni, T.; Rizzo, A.; Calestani, G.; Gigli, G.; De Angelis, F.; Mosca, R. *Chemistry of Materials* **2013**, *25*, 4613–4618.
- (31) Uratani, H.; Yamashita, K. *Journal of Physical Chemistry Letters* **2017**, *8*, 742–746.
- (32) Herz, L. M. **2016**,
- (33) Filip, M. R.; Eperon, G. E.; Snaith, H. J.; Giustino, F. *Nature Communications* **2014**, *5*, 5757.
- (34) Sutton, R. J.; Zampetti, A. *Journal of Materials Chemistry A* **2015**, *3*, 19688–19695.
- (35) Unger, E. L.; Kegelmann, L.; Suchan, K.; S?rell, D.; Korte, L.; Albrecht, S. *J. Mater. Chem. A* **2017**, *5*, 11401–11409.

- (36) others,, et al. *Journal of physics: Condensed matter* **2009**, *21*, 395502.
- (37) Perdew, J. P.; Burke, K.; Ernzerhof, M. *Phys. Rev. Lett.* **1997**, *78*, 1396–1396.
- (38) Garrity, K. F.; Bennett, J. W.; Rabe, K. M.; Vanderbilt, D. *Computational Materials Science* **2014**, *81*, 446–452.
- (39) Madsen, G. K. H.; Singh, D. J. **2006**, *175*, 67–71.
- (40) Zhao, T.; Shi, W.; Xi, J.; Wang, D.; Shuai, Z. *Scientific Reports* **2016**, *7*, 19968.
- (41) Lee, M.-S.; Poudeu, F. P.; Mahanti, S. *Physical Review B* **2011**, *83*, 085204.
- (42) Motta, C.; El-mellouhi, F.; Sanvito, S. *Nature Publishing Group* **2015**, 1–8.
- (43) Liu, J.; Prezhdo, O. V. *Journal of Physical Chemistry Letters* **2015**, *6*, 4463–4469.
- (44) Wehrenfennig, C.; Eperon, G. E.; Johnston, M. B.; Snaith, H. J.; Herz, L. M. *Advanced Materials* **2014**, *26*, 1584–1589.
- (45) Geng, W.; Tong, C.-J.; Liu, J.; Zhu, W.; Lau, W.-M.; Liu, L.-M. *Scientific Reports* **2016**, *6*, 20131.
- (46) Mosconi, E.; Ronca, E.; De Angelis, F. *The Journal of Physical Chemistry Letters* **2014**, *5*, 2619–2625.
- (47) Long, R.; Prezhdo, O. V. *ACS Nano* **2015**, *9*, 11143–11155.
- (48) Long, R.; Fang, W. H.; Prezhdo, O. V. *Journal of Physical Chemistry C* **2017**, *121*, 3797–3806.
- (49) Tripathi, N.; Yanagida, M.; Shirai, Y.; Masuda, T.; Han, L.; Miyano, K.; Mater, J.; Chem, a.; Tripathi, N.; Yanagida, M.; Shirai, Y.; Masuda, T.; Han, L.; Miyano, K. *Journal of Materials Chemistry A: Materials for energy and sustainability* **2015**, *3*, 12081–12088.

Combining Optical Imaging with MRI

DiTusa, Rebecca

Abstract— Functional/Magnetic Resonance Imaging (f/MRI) systems have aided in medical research through the use of large field-of-view (FOV) imaging. However, high resolution, small FOV imaging would enhance the ability to analyze systems on a smaller, cellular scale. Two-photon microscopy has been used for deep-image small FOVs without a surgical procedure—but simultaneously achieving an MRI scan is difficult. Although scanning separately is achievable, it lacks the ability to definitively correlate events between scans due to the difference in time. In order to image a small and large FOV concurrently, a microscope constructed out of MRI-safe material is needed. To achieve this parameter, piezoelectric materials are used. They are MRI compatible and by using multiple orientations, motion in more than one dimension is possible.

I. INTRODUCTION

IMAGING the brain is often attained by a Magnetic Resonance Imaging (MRI) scan.

Typically, this type of scan is used to image large structures in the body. To obtain this, a superconducting solenoid is placed around an object of interest. Electric current is used to create a magnetic field—by introducing a strong magnetic field, most of hydrogen’s magnetic moments inside the solenoid align with the magnetic field. Once they are aligned, a new magnetic field—which changes the direction of the magnetic moments—is applied and then turned off. The amount of time it takes for the magnetic moments to point in its original direction is measured. Also, by introducing radio waves and exciting molecules and measuring the amount of time it takes for the molecule to go back to its ground state—by emitting a photon—is measured. Both of the times measured aid in creating an image that helps differentiate between materials in the body.

In a similar manner, a functional MRI (fMRI) is typically used to image blood flow in the brain. Instead of imaging neurons firing, the blood-oxygen level dependent (BOLD) effect is imaged. The BOLD effect takes advantage of the fact that oxygenated hemoglobin (protein that transports oxygen) is diamagnetic and deoxygenated hemoglobin is paramagnetic. This means that oxygenated hemoglobin’s magnetic moments typically do not align with the magnetic field, and deoxygenated hemoglobin’s magnetic moments do align—allowing a measurable difference between the two.

Although both MRI and fMRI allow for useful information to be obtained on a large field of view (FOV)/whole structures, they lack the ability to image small FOVs. A small FOV would be useful to examine the structure and function on a cellular level—giving insight on how and why neurological diseases occur.

Instead, photon microscopy allows small FOV imaging. Photon microscopy starts with a high-pulsed laser that excites molecules. The excited molecules de-excite and the emitted photon is obtained to create an image. Compared to one-photon microscopy, two-photon microscopy allows for non-invasive and deeper imaging. Two-photon microscopy also starts with a high pulse laser, but instead uses photons with half the amount of energy. By sending in lower energy photons, the risk of damaging cells decreases and a greater imaging depth can be achieved, due to fewer unwanted interactions. Another benefit to two-photon microscopy is that as the photons converge at the focal point, the density of photons becomes greater. Since the laser pulses are on the order of femtoseconds, when the two photons are absorbed at the focal point, the absorption was so close in time that upon de-exciting, only one photon is emitted—this photon has the same amount of energy as an emitted photon in one photon microscopy. And unlike in fMRI, photon microscopy will image neurons firing, rather than oxygen in the blood.

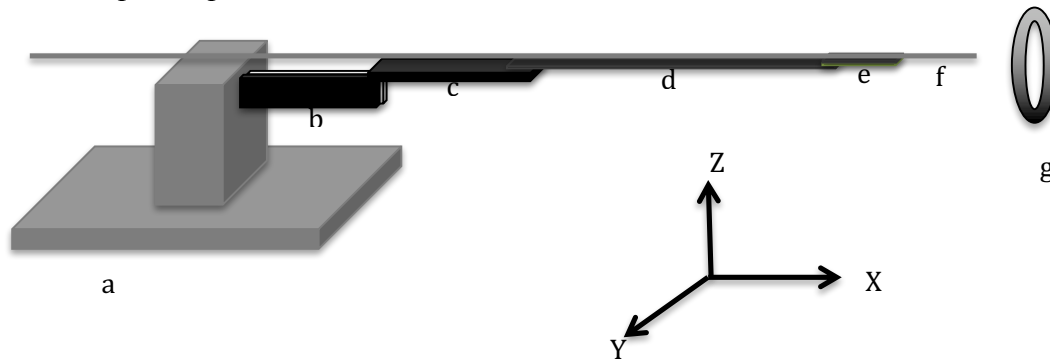
Combining two-photon microscopy and fMRI would allow for imaging whole organs as well as on the cellular level at the same time. Although this would lead to medical advancements, there are challenges that must be overcome before this is attainable. Since MRIs are made out of a superconducting magnet that cannot be turned off, ferromagnetic metals may not be used in or near an MRI. Since their magnetic moments are fixed, a torque would be produced and the object would be strongly attracted to the center of the solenoid. Microscopes are typically made out of ferromagnetic metals and therefore would not work inside an MRI—so one can determine what is happening on a cellular level before or after a scan, but not during.

II. PROCEDURE

In order to get a microscope that has no ferromagnetic metal but still has motion, piezoelectric materials are used. A trimorph piezoelectric is a quartz crystal in the middle of two pieces of ceramics that converts electrical energy into kinetic energy. When voltage is applied to one side of the piezo, that side expands and the other side stays the same length, so bending occurs. Then when the voltage is no longer applied, it goes back to its equilibrium position, where both pieces of ceramic are the same size and there is no more bending. Then, if voltage is applied to the other side, the piezo will bend in the opposite direction. Piezos are not ferromagnetic and therefore can go inside of an MRI.

Another item used for imaging is the lens, which will be held by a piece of brass. In order to power the scanner, a voltage amplifier and a function generator must be used—materials that cannot be present in the same room as an MRI. With the amplifier and function generator in a separate room, copper electrical wires (non-ferromagnetic) are connected to the piezos.

Microscope setup



* = length

a: Plexiglas stand

b: first piezo oriented in the xz axis—therefore moves in the y direction *20mm

c: second piezo oriented in the xy axis—therefore moves in the z direction *14mm

d: carbon fiber tube *70mm

e: third piezo oriented in the xy axis—therefore moves in the z direction *5mm

f: fiberglass—transfers pulses from laser to object in MRI and emitted light from object to an imaging system *9.5mm

g: brass lens holder

To attain greatest deflection/largest image parameters in one dimension and fastest imaging, the fibers length and shape needs to be experimented with. For example, for the fiber to move in one dimension, i.e. up and down, the symmetry needs to be broken. One way to break the symmetry would be to glue two fibers side by side. Another way to break the symmetry would be to glue three fibers together in a triangle. Also, by changing the radius of the fiber, the deflection and frequency changes. So to find a good balance, different combinations are tested.

Fiber arrangements:



Combinations with 130μm fiber and:

- 125μm, 130μm, 400μm, and 900μm
- With an overhang of 5 mm, 7 mm, and 9 mm

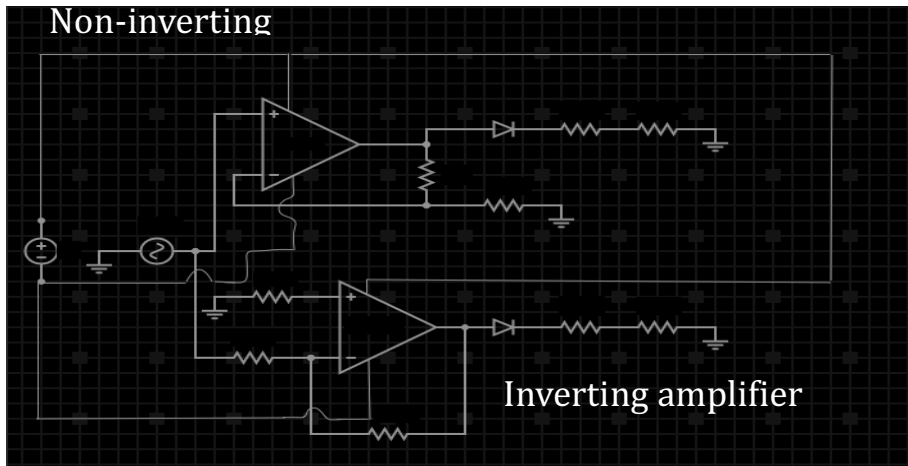
Frequency and deflection equations:

$$\nu = \frac{\beta R}{4\pi L^2} \sqrt{\frac{E}{\rho}}$$

$$D = 2c(L_1^2 + 2L_1L_2) \times \left(\frac{V_{\text{applied}}}{V_{\text{spec}}} \right)$$

- The longer the fiber = the greater the deflection but lower the frequency
- The larger the radius = higher the frequency but lower the deflection

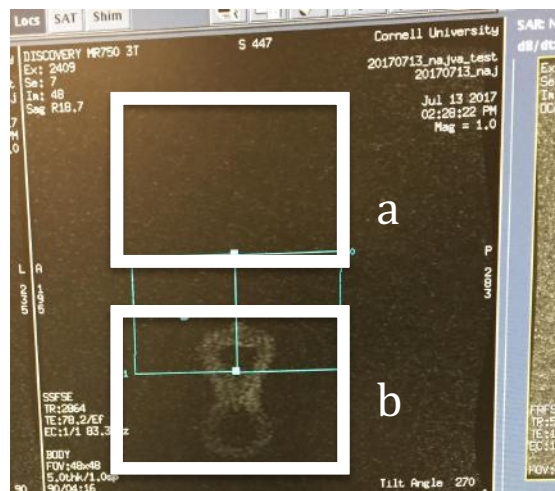
In order to power the piezos without destroying its properties, the voltage must always be positive. So, a circuit with an inverting amplifier and a non-inverting amplifier with diodes must be constructed.



Each piezo will need one of these circuits. The non-inverting part of the circuit will be connected to one side of the piezo; the inverting amplifier is connected to the other side. By connecting each to a different side of the piezo, a cyclical motion of up-and-down—or side-to-side—can transpire. The first two piezos can be driven at any frequency, but the third piezo needs to be driven at the resonant frequency of the fiber in order to get the greatest deflection. The ideal frequency is 4kHz and the desired deflection is >3mm.

III. RESULTS

The circuit pictured above was able to move the piezos in the anticipated way. Once the piezo scanner was placed inside of an MRI, regular imaging was implemented with no disruptions. Also, the piezo scanner was able to consistently move throughout the scan.

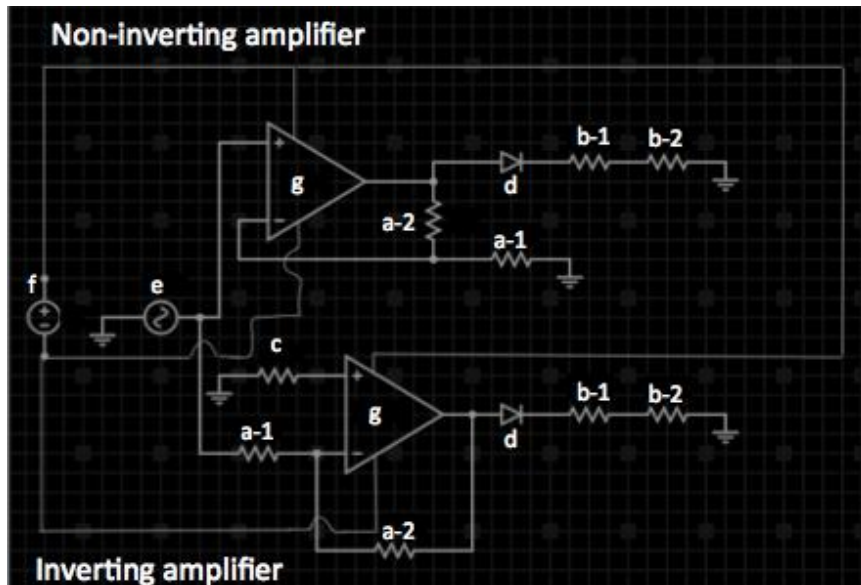


box a: cannot see the piezo scanner
 box b: squash imaged without disruption caused from piezo scanner

The best fiber deflection and frequency was achieved when two 125 μm and one 215 μm fiber was glued together in a triangle configuration and had a length of 7mm. The resonant frequency was 3.5kHz and the deflection was 1 mm.

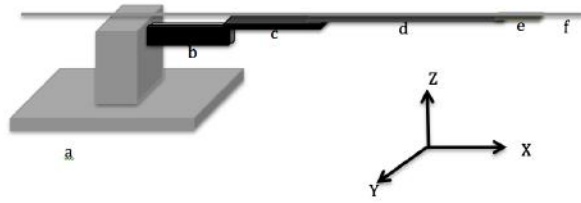
The non-inverting and inverting circuits need to have very large resistors in order to lower the current to drive the piezo scanner. Many different combinations of resistors were tested with in order to find values that worked with the piezos.

Inverting and non-inverting amplifying circuit:



Circuit Elements	Explanation
a-1: 12k Ω resistor a-2: 503k Ω resistor	To create a gain of 40
b-1: 33k Ω resistor b-2: 3.3k Ω resistor	Voltage divider to determine voltage with function generator—for troubleshooting
c: 100 Ω resistor	To create an inverting
d: Ultrafast rectifier	To create only a positive output to power piezos
e: function generator	Applying a voltage for 10 volts peak-to-peak in order to create 200 volts going to op-amp from the gain of 40 coming from op-amps
f: Amplifier	Supplying 250 volts to op-amp voltage source
c: High power MOSFET op-amp	To amplify signal

The theoretical deflection was compared to the experimental deflection:



Scanner number	b (mm)	c (mm)	d (mm) (+/- 0.5mm)	Third piece (mm)	e (mm)	Fiber (mm)	Fiber	b deflection (mm)	Theoretical deflection of fiber tip (mm)	c deflection (mm)	Theoretical deflection of fiber (mm)	d deflection (3rd piezo, only for scanner 1)	Theoretical deflection of fiber tip (mm)	e experimental deflection (fiber) (mm)	Resonant Frequency (kHz)
1	39	43	0.5	28	5	9	125 μ m & 125 μ m	6.5	15.8052632	5	10.589197	3	3.04044321	3.5	0.595
2	20	14	0.5	69.5	5	9.5	2 fibers: 130 & 215 μ m	4	8.41551247	3	4.9407202	-----	-----	1	1.85
3	21	28	0.5	70	5	8	2 fibers: 130 & 215 μ m	5.5	9.93573407	5	10.532964	-----	-----	1	1.254
4	21	19	0.5	80	8	8	125 μ m & 125 μ m	6.5	10.2614958	3	7.7736842	-----	-----	3	1.408

Note: grey boxes show the theoretical deflection is about twice as much as the experimental deflection for first two piezos

IV. DISCUSSION

While the resonant frequency of the new fiber arrangement is at 3.5kHz—which is about 1.5kHz higher than what was achieved with two 125 μ m fibers—the deflection decreases by about one-third. The preferred resonant frequency is 4kHz with a deflection of >3mm. Frequency of the fiber is proportional to the radius of the fiber divided by the length of the fiber squared. So the smaller the fiber, the higher the frequency. But, deflection is proportional to the lengths of the fibers—so the longer the fiber is, more deflection can be attained.

When connecting the circuit to the piezo scanner, the deflection is about half of the theoretical deflection. Although the gain is 40x with the chosen resistors, the gain is measured to be more than expected, which may result in a lower deflection.

V. CONCLUSION

With the MRI, a large field of view is imaged and with two-photon microscopy, a small field of view is achievable. The experimental piezo scanner is able to achieve a 4mm deflection in the y-axis and a 3mm deflection in the z-axis; the fiber on the third piezo is able to attain about a 1mm deflection at 3.5kHz. The two larger piezos can be powered at any frequency that is needed. The last piezo must be powered with a frequency at its resonant to ensure the best deflection of the fiber. So overall, a two-dimensional scanner has been constructed with the ability to image a small field of view in an MRI. By gluing two different sized fibers together in a triangle arrangement, greater frequency is achieved, but lacks the preferred deflection. Then, with a non-inverting and inverting amplifying circuit, powering the piezo scanner is achieved—without destroying the piezo's properties. Through experimentation of a piezo scanner in an MRI, it has been proven that both can exist in the same area and function as desired. In the future, by

combining the piezo scanner in an MRI while imaging a live mouse, connections between neurological diseases can be obtained. And with this information, further experimentation to cure neurological diseases can occur.